Mesoscopic in vivo human T_2^* dataset acquired using quantitative MRI at 7 Tesla

Omer Faruk Gulban[1]
Dep. of Cognitive Neuroscience
FPN, Maastricht University
Maastricht, Netherlands

Saskia Bollmann
Centre for Advanced Imaging
The University of Queensland
Brisbane, Australia

Renzo Huber
Dep. of Cognitive Neuroscience
FPN, Maastricht University
Maastricht, Netherlands

Konrad Wagstyl
Wellcome Centre for Human
Neuroimaging, UCL
London, UK

Rainer Goebel
Dep. of Cognitive Neuroscience
FPN, Maastricht University
Maastricht, Netherlands

Benedikt A. Poser
Dep. of Cognitive Neuroscience
FPN, Maastricht University
Maastricht, Netherlands

Kendrick Kay[2]
CMRR, Dep. of Radiology
University of Minnesota
Minneapolis, USA

Dimo Ivanov[2]
Dep. of Cognitive Neuroscience
FPN, Maastricht University
Maastricht, Netherlands

July 29, 2022

ABSTRACT

Mesoscopic (0.1-0.5 mm) interrogation of the living human brain is critical for advancing neuroscience and bridging the resolution gap with animal models. Despite the variety of MRI contrasts measured in recent years at the mesoscopic scale, in vivo quantitative imaging of T_2^* has not been performed. Here we provide a dataset containing empirical T_2^* measurements acquired at $0.35 \times 0.35 \times 0.35$ mm^3 voxel resolution using 7 Tesla MRI. To demonstrate unique features and high quality of this dataset, we generate flat map visualizations that reveal fine-scale cortical substructures such as layers and vessels, and we report quantitative depth-dependent T_2^* values in primary visual cortex and auditory cortex that are highly consistent across subjects. This dataset is freely available at `https://doi.org/10.17605/OSF.IO/N5BJ7`, and may prove useful for anatomical investigations of the human brain, as well as for improving our understanding of the basis of the T_2^* -weighted (f)MRI signal.

Keywords in vivo · human · MRI · 7 T · mesoscopic · T_2^* · brain · cortex · layers · vessels · visual · auditory · cortex · angioarchitecture

[1]Corresponding author (`https://orcid.org/0000-0001-7761-3727`).
[2]Equal contribution.

1 Introduction

A central goal in neuroscience is to achieve a comprehensive assessment of the structure of the living human brain. Centuries of work have been dedicated to characterizing the human brain from its macroscopic features (e.g., lobes, gyri, sulci) to its microscopic constituents (e.g., dendrites, cell bodies) (Finger et al., 2009, Ch. 1-10). The history of neuroscience has witnessed steady improvements in technologies for imaging the brain at increasing levels of detail (Bentivoglio & Mazzarello, 2009). From the late 19th to the early 20th century, major advancements in tissue staining and photography opened new doors for measuring the human brain's cytoarchitecture (Geyer, 2013, Part 1), myeloarchitecture (Nieuwenhuys, 2013), fiber architecture (Kleinnijenhuis, 2014, Ch. 1), and angioarchitecture (Pfeifer, 1940).

In seminal works of neuroscience, it has been acknowledged that post mortem experiments on animal and human brains are valuable but temporary necessities (Stahnisch, 2010). Fortunately, new technologies that enable study of the living human brain have emerged. The second half of the 20th century has brought computerized tomography (CT), positron emission tomography (PET), and magnetic resonance imaging (MRI) (Raichle, 2009a). Though these new technologies were far from the microscopic details provided by older methods, they quickly became indispensable due to their non-invasive nature. MRI has proven particularly useful for its flexibility to measure different tissue contrasts as well as hemodynamic measures of brain activity (Raichle, 2009b). Recently, MRI at ultra-high magnetic field strength ($\geq$7 Tesla) has breached the mesoscopic scale, which we define as resolutions between 0.1 mm and 0.5 mm (Edwards et al., 2018). Particularly, openly accessible datasets by Bollmann et al. (2022), Federau and Gallichan (2016), Lüsebrink et al. (2021), and Lüsebrink et al. (2017), Schira et al. (2022) have facilitated the incorporation of mesoscopic MRI into the toolkit of practicing neuroscientists. However, despite the rich variety of MRI contrasts acquired by the previous work (Barbier et al., 2002; Bollmann et al., 2022; Bridge et al., 2005; Budde et al., 2011; Dinse et al., 2015; Duyn et al., 2007; Federau & Gallichan, 2016; Fracasso et al., 2016; Kemper et al., 2018; Lüsebrink et al., 2021; Lüsebrink et al., 2017; Mattern et al., 2018; Petridou et al., 2010; Sanchez Panchuelo et al., 2021a; Sánchez-Panchuelo et al., 2012; Schira et al., 2022; Tardif et al., 2015; Trampel et al., 2011; Turner et al., 2008; Zwanenburg et al., 2011), there has been no openly accessible quantitative in vivo human T_2^* measurements at mesoscopic resolution (see **Supplementary Table 1**).

In this paper, we deliver this missing element: quantitative in vivo human T_2^* measurements. The data are acquired at the challenging resolution of $0.35 \times 0.35 \times 0.35$ mm^3 voxels at 7 Tesla and cover a substantial portion (approximately one-third) of the human brain, primarily including the visual and auditory cortices. To highlight the unique features and high quality of this dataset, (i) we provide a local (voxel-wise) qualitative assessment of cortical substructures using three dimensional flat maps, highlighting cortical substructures such as layers and vessels; and (ii) we provide a global (region-of-interest-wise) quantitative report of depth-dependent (also referred as layer-dependent) T_2^* values of the cortical gray matter, superficial white matter, and above pial surface at the primary visual and auditory cortices.

2 Methods

2.1 Participants

Five healthy participants (2 females, 27-35 years old) were recruited for the study. These participants were selected for their experience in participating in 7 T experiments and for their ability to keep their heads still for a long time. Similar preselection strategies were previously used in high resolution MRI studies (Allen et al., 2022; Bollmann et al., 2022; Tardif et al., 2015). Informed consent was obtained from each participant before conducting the experiment. The study was approved by the research ethics committee of the Faculty of Psychology and Neuroscience of Maastricht University and experimental procedures followed the principles expressed in the Declaration of Helsinki.

2.2 Data Acquisition

2.2.1 Session 1: T_2^* with ME GRE

In the first session, we acquired 3D multi-echo gradient recalled echo (ME GRE) images with bipolar readouts (Eckstein et al., 2018) to measure T_2^* (see **Table 1**) using 7T MRI (Siemens) with a 32-channel Rx head coil (Nova). The nominal image resolution was $0.35 \times 0.35 \times 0.35$ mm^3, and parameters included TR = 30 ms, $TE_{1\text{-}6}$ = [3.83, 8.20, 12.57, 16.94, 21.31, 25.68] ms, FA = 11°, $576 \times 576 \times 104$ voxels, FOV = $20.16 \times 20.16 \times 3.64$ cm^3, GRAPPA = 2, elliptic k-space filling, 15 minutes duration, and no flow compensation. See **Figure 1** for the positioning of our imaging slab. Four successful ME GRE runs totalling 60 minutes were acquired in this scanning session. Between acquisitions of the 3D ME GRE we changed the phase-encoding direction by 90° (right-left, anterior-posterior, left-right, posterior-anterior). These 90° changes were introduced in order to control the direction of the blood motion artifact which is caused by

Table 1: Acquisition parameters for the high-resolution scanning protocols (7 T MRI).

Sequence	ME GRE	MP2RAGE
Voxel size	$0.35 \times 0.35 \times 0.35$ mm^3	$0.35 \times 0.35 \times 0.35$ mm^3
Field of view (FOV)	$201.6 \times 201.6 \times 36.4$ mm^3	$201.6 \times 201.6 \times 42$ mm^3
Slab dimensions	$576 \times 576 \times 104$ voxels	$576 \times 576 \times 120$ voxels
Bandwidth	240 Hz/Px	250 Hz/Px
TR	30 ms	5000 ms
TE	[3.83, 8.20, 12.57, 16.94, 21.31, 25.68] ms	2.91 ms
Flip angle (FA)	11°	[4°, 5°]
TI	N/A	[800, 2700] ms
Read-out gradient mode	Bipolar	Monopolar
Phase partial Fourier	Off	6/8
GRAPPA	2	2
Volume acquisition time	15 min	10 min
Total duration	4×15 min = 60 min	6×10 min = 60 min

the time difference between the phase encoding and readout stages (this artifact is called "spatial misregistration of the vascular flow" by Larson et al., 1990). As a result of this blood motion artifact, we see the vector component of the blood flow in the readout direction as a displacement (see **Supplementary Figure 1**). Additionally, the bipolar readouts have odd- and even-numbered echos acquired with opposite (180°) readout directions, which is known to introduce a slight spatial shift between their corresponding images due to the change in readout direction (Cohen-Adad, 2014). However, we found that this shift is negligible compared to the blood motion artifact. We have also acquired a whole-brain magnetization prepared 2 rapid acquisition gradient echos (MP2RAGE) image (Marques et al., 2010) at 0.7 mm isotropic resolution. Parameters of this whole-brain MP2RAGE acquisition was TR = 5000 ms, $TI_{1\text{-}2}$ = [900, 2750] ms, TE = 2.46 ms, $FA_{1\text{-}2}$ = [5°, 3°], $320 \times 320 \times 240$ voxels, FOV = $22.4 \times 22.4 \times 16.8$ cm^3.

2.2.2 Session 2: T_1 with MP2RAGE

In the second session, we acquired mesoscopic MP2RAGE images (Marques et al., 2010) (see **Table 1**) the same setup with the same participants. These T_1 data were acquired primarily for cortical gray matter segmentation purposes and were not intended to serve as quantitative T_1 measurement. The nominal image resolution was equal to the T_2^* images at $0.35 \times 0.35 \times 0.35$ mm^3, and parameters included TR = 5000 ms, TE = 2.91 ms, $TI_{1\text{-}2}$ = [800, 2700] ms, $FA_{1\text{-}2}$ = [4°, 5°], $576 \times 576 \times 120$ voxels, $20.16 \times 20.16 \times 4.2$ cm^3 slab dimensions, GRAPPA = 2, Partial Fourier = 6/8, Bandwidth = 250 Hz/Px, and 10 minutes duration. See **Figure 1A** for the positioning of our imaging slab. Six successful MP2RAGE runs totalling 60 minutes were acquired in this scanning session. For completeness, we changed the phase-encoding direction by 90° in each run similar to the ME GRE images acquired in Session 1. However, the effect of the blood motion artifact was negligible because of the short TE used in MP2RAGE images compared to ME GRE.

2.3 Data Analysis

Data processing and analysis scripts referenced in this section are available at: `https://github.com/ofgulban/meso-MRI`.

2.3.1 T_2^* Images (ME GRE)

Each ME GRE image series consists of odd- and even-numbered echos with opposite readout direction (while phase-encoding was rotated by 90° between acquisitions). Our processing pipeline aimed at reducing two sources of artifacts while improving the signal-to-noise ratio: (i) head motion across acquisitions, (ii) blood motion artifacts across echos. The processed data is then used to compute T_2^* and S_0 values. Note that we did not need to deface our images as face region is not included in our imaging slab to begin with. See **Supplementary Figure 2** for an overview of the preprocessed data quality across participants which shows that the fine detailed cortical substructures are captured consistently across all participants.

2.3.2 Head motion correction

There are two types of bulk head motion to consider: (i) "within-run head motion" which introduces blur and ringing artifacts into the images, and (ii) "in between runs" head motion which blurs the average of images. To address the

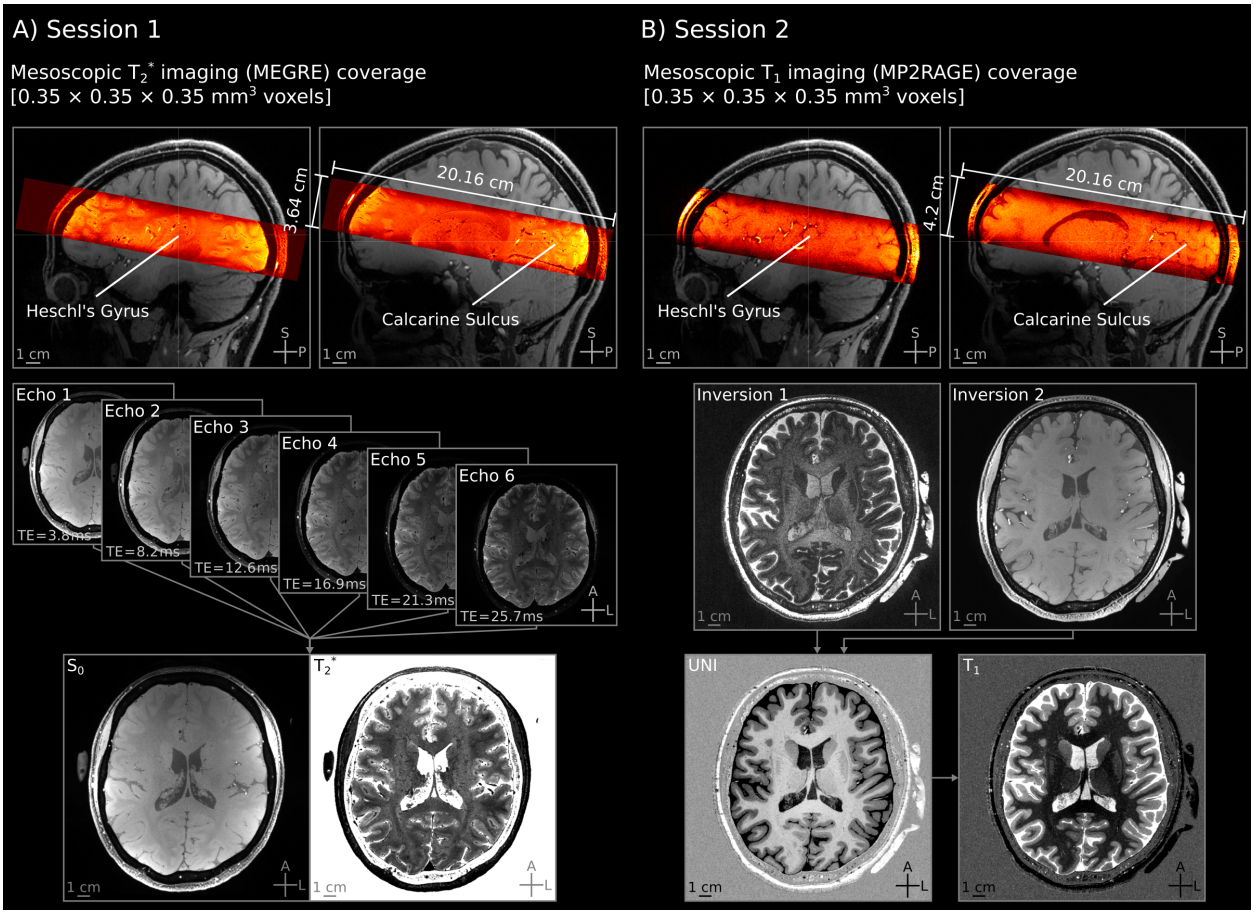

Figure 1: Spatial coverage and image quality of the MRI data acquisition. Here we show data quality for an example participant (sub-01) for the first **(A)** and second scan sessions **(B)** after preprocessing. High-resolution imaging slabs (in warm colors) are overlaid on top of the whole-brain lower-resolution image. The imaging slabs are positioned to cover both the calcarine sulci and Heschl's gyri (transverse temporal gyrus). Transversal images are averaged across runs. Despite the very high spatial resolution (0.35 mm isotropic), SNR of our averaged images is high, clearly showing fine details in each individual (see **Supplementary Figures 2**) and the SNR of individual runs are consistent across acquisitions (see **Supplementary Figures 3-4**). See **Table 1** for acquisition parameters, and **Section 2.8** for data availability and sequence parameter documents.

within-run head motion, we preselected participants who are experienced with being scanned and with minimizing head motion. This strategy has been used successfully in Allen et al. (2022), Bollmann et al. (2022), and Tardif et al. (2015). In addition, we kept our run durations between 10-15 minutes. Durations above 20 minutes have been shown to require prospective motion correction (Lüsebrink et al., 2017; Mattern et al., 2018; Stucht et al., 2015), or the use of fat-based motion navigators (Federau & Gallichan, 2016; Gallichan et al., 2016). However, shorter acquisition durations together with participant preselection has been shown to generate similar quality data up to 0.16 mm isotropic resolution (Bollmann et al., 2022). While Bollmann et al. (2022) reports approximately 1 out of 4 runs had to be discarded, we did not discard any data upon quality controlling our images. An overview of our unpreprocessed data in **Supplementary Figure 3** shows the effectiveness of our participant preselection strategy yielding high quality images that are not strongly affected by within run head motion in any of the individual runs.

We started by cropping our images to exclude the frontal brain regions (`01_crop.py`). This is done to reduce computational requirements for the upcoming steps. Then we averaged signal intensities across all echos per voxel (`02_avg_echos.py`). This averaged image improves SNR and is used only in the estimation of motion. We also upsampled both the original echos and the averaged images to 0.175 mm isotropic resolution with cubic interpolation; this allows fine-scale detail to be preserved during the motion correction process (**Allen2021**) (`03_upsample.py`). Head motion was estimated from the averaged images using rigid-body transformation (6 degrees of freedom) while using a manually defined brain mask covering our regions of interest; then, data were corrected using linear in-

terpolation (`04_motion_correct.py`) (Yushkevich et al., 2006). Note that all runs are co-registered to the first ME GRE run. The estimated rigid body transformation matrices were applied to each upsampled echo separately (`05_split_echos.py, 07_apply_reg.py, 08_merge_echos.py`), resulting in a final set of brain volumes with nominal 0.175 mm resolution.

2.3.3 Blood motion artifact mitigation

After motion correction, we averaged the ME GRE images with the same phase-encoding axis for each echo (PE_x for right-left and left-right; PE_y for anterior-posterior and posterior-anterior) to improve signal-to-noise ratio (`09_average_same_PE_axes.py`). This step is performed because the blood motion artifact direction is independent of the *phase-encoding direction*, and only dependent on the *vector component of the blood flow along the readout axis* (Larson et al., 1990). Then we composited a new image by selecting voxels from the PE_x and PE_y phase encoding axis images using a minimum operator (`10_composite.py`). Selecting the minimum intensity observed across the two images mitigates the blood motion artifact. Such image compositing operations are commonly used in the movie-making visual effects field (Brinkmann, 2008). In compositing, the main idea is to piece together a new image by using parts of multiple other images (see **Supplementary Figure 1**). Since the blood motion artifact will be different across images with 90° rotated phase-encoding axes (PE_x and PE_y), it is conceivable to composite a new image (i.e. a new set of echos) by selecting the signal of each voxel from the original set that is not affected by the artifact (a voxel affected by the artifact in PE_x will not be affected in PE_y). As the last step to mitigate the residual blood motion artifacts, we detected those voxels that do not decay across echos (e.g. points on the decay curve showing a higher signal compared to the echo that comes before), and replaced its value with an average of the echo before and after (`11_fix_nondecay.py`). Note that our procedure is best viewed as *mitigating* as opposed to *correcting* the blood motion artifact: we are attempting to suppress the misencoded artery signal, not move it back to its correct location. We also highlight that we used the minimum operator as the simplest way of mitigating the blood motion artifact. Alternative artifact-mitigation strategies that might more efficiently combine the data constitute an interesting direction for future work.

2.3.4 T_2^* fitting

We fit a monoexponential decay function ($S_{TE} = S_0 \cdot \exp(-TE/T_2^*)$) to the processed ME GRE images by fitting a line to the logarithm of the signal using ordinary least-squares (`12_fit_T2star.py`) (Cohen-Adad et al., 2012) using Nibabel, Scipy, and Numpy (Brett et al., 2017; Jones et al., 2001; Van Der Walt et al., 2011). Note that in addition to providing an estimate of T_2^*, this procedure also provides an estimate of S_0 (see **Figure 1**).

2.4 T_1 Images (MP2RAGE)

Our processing strategy for the T_1 images is aimed at correcting head motion across acquisitions while boosting signal-to-noise ratio through averaging. Note that we did not need to deface our images as face region is not included in our coverage to begin with. See **Supplementary Figure 4** for an overview of the preprocessed data quality across participants which shows that we have attained a good contrast to delineate the inner and outer boundaries of the cortical gray matter.

2.4.1 Head motion correction

Similar to T_2^* (ME GRE) data, no data was discarded. An overview of our data before any preprocessing can be seen in **Supplementary Figure 4**, which shows that similarly to the T_2^* (ME GRE) imaging, our participant preselection strategy was effective to mitigate the within run bulk head motion artifacts, yielding good quality images that are ready for coregistration followed by averaging to boost signal-to-noise ratio.

MP2RAGE images were processed similarly to the ME GRE images for the first two steps of cropping and upsampling (`01_crop.py, 02_upsample.py`). All runs are co-registered to the first MP2RAGE run using the second inversion time (INV2) contrast with the GREEDY (Yushkevich et al., 2016) registration algorithm (acquired from: `https://github.com/pyushkevich/greedy`). We used the second inversion time contrast to drive registration because it has the best overall brain and non-brain signal-to-noise ratio. A brain mask focusing on our regions of interest was manually drawn in ITK-SNAP (Yushkevich et al., 2006) and used to constrain the registration cost metric. Registration was estimated using GREEDY rigid-body transformation (6 degrees of freedom) and data were corrected using linear interpolation (`03_motion_correct.py`). The estimated transformations were applied to all of the MP2RAGE contrasts (`04_apply_reg.py`). Finally, we computed the average across all motion-corrected images (`05_average.py`).

2.4.2 Registration to T_2^*

The MP2RAGE data were registered to the ME GRE using the second inversion time (INV2) contrast from the MP2RAGE and the S_0 image resulting from T_2^* fitting of the ME GRE. This choice was made due to the similarity of tissue contrast in these images. We used the GREEDY registration with 6 degrees of freedom and linear interpolation (`06_register_to_T2s.py`).

2.5 Segmentation

Accurate identification of gray and white matter is critical for proper interpretation of cortical architecture. We carefully segmented four main regions of interest in the registered MP2RAGE UNI images. These regions consisted of brain tissue in and around the calcarine sulcus and Heschl's gyrus in each hemisphere. To determine these regions, we centered a spherical mask at each of the relevant sulcal and gyral landmarks. We refer to these masks as "scoops of interest" (see **Figure 2**). We used an interactive intensity histogram thresholding method (Gulban et al., 2018) to obtain our initial tissue segmentation within each scoop of interest based on the MP2RAGE UNI contrast. After this step, each scoop of interest was manually edited by an expert (O.F.G.) and quality controlled for accurate and precise tissue segmentation (R.H.). The manual editing process took approximately 8 to 10 hours for each subject. We have chosen this laborious manual segmentation process over a fully automatic one because of the lack of optimized and validated segmentation tools for our very high resolution data. The resulting tissue segmentations are available as a part of our data repository and can be freely inspected or used for validating the results of automatic algorithms (Bazin et al., 2014; Svanera et al., 2021). Note that we used the scoops of interest rather than segmenting all of the brain tissue available within our imaging slabs to focus our efforts on achieving the best segmentation for our regions of interest.

2.6 Cortical Depths

After completing the tissue segmentation, we used LayNii v.2.2.0 (Huber et al., 2021) to compute equi-volume cortical depths (Bok, 1959). Specifically, we prepared the segmentation input, i.e. the motion-corrected and averaged T_1 -weighted images (`00_prep.py`), and used the LN2_LAYERS program to compute equi-volume normalized cortical depth measurements for each gray matter voxel (`01_layers.py`). Note that the voxel-wise cortical depth metric computed in LN2_LAYERS ranges between 0 and 1 and reflect normalized units: cortical depth measurements (in mm) are normalized by local cortical thickness measurements (in mm) and then adjusted within this closed vector space to determine the equi-volume metric (see **Figure 2B** and **Figure 3B**) (this implementation is described in Huber et al., 2021). In addition, this program computes cortical curvature at each gray-matter voxel. See (Bok, 1959; Waehnert et al., 2014) for general references on the equi-volume principle of cortical layering.

To facilitate anatomical quantification, we also calculated distances for voxels that lie beyond the inner and outer gray-matter boundaries. This was done using LayNii program LN2_GEODISTANCE (`02_beyond_gm_prep.py, 03_beyond_gm_distances.py`). These beyond-gray-matter distances are quantified in mm units and we included voxels that are maximally 0.75 mm away from any gray matter border. Then, we created a collated distance file, combining the equi-volume depth metric together with the beyond-gray-matter distances (`04_beyond_gm_collate.py, 05_beyond_gm_stitch.py`). This file is used to plot cortical depth profiles together with voxels above and below the gray matter in **Figures 6-7** and **Figures A.1-A.2** (`01_singlesub_depth_vs_T2star.py, 02_singlesub_depth_vs_T1.py, 01_group_depth_vs_T2star.py, 01_group_depth_vs_T1.py`) using Matplotlib (Hunter, 2007).

2.7 Flat Maps

We first used LayNii v2.2.0 LN2_MULTILATERATE program to inject a local coordinate system within our segmented regions (`01_multilaterate.py`). This local coordinate system is abbreviated with U and V coordinates, which are visible in **Figure 3A**. We then used LN2_PATCH_FLATTEN program to combine the voxel-wise UV coordinates with the equi-volume cortical depth measurements (abbreviated as D coordinate, see **Figure 3B**) to flatten cylindrical (30 mm in diameter) cortical patches within our regions-of-interest (`02_patch_flatten.py`). The end result of this procedure is a full continuous mapping between flat cortex space (UVD) and the original folded cortex space (XYZ) (see **Figure 3**).

2.8 Data and Code Availability

Unprocessed data, sequence parameters (PDFs), and part of the processed data (due to data storage constraints) used in this study are available at: `https://doi.org/10.17605/OSF.IO/N5BJ7` under "Data" folder. Processing and analysis scripts used in this study are available at: `https://github.com/ofgulban/meso-MRI`.

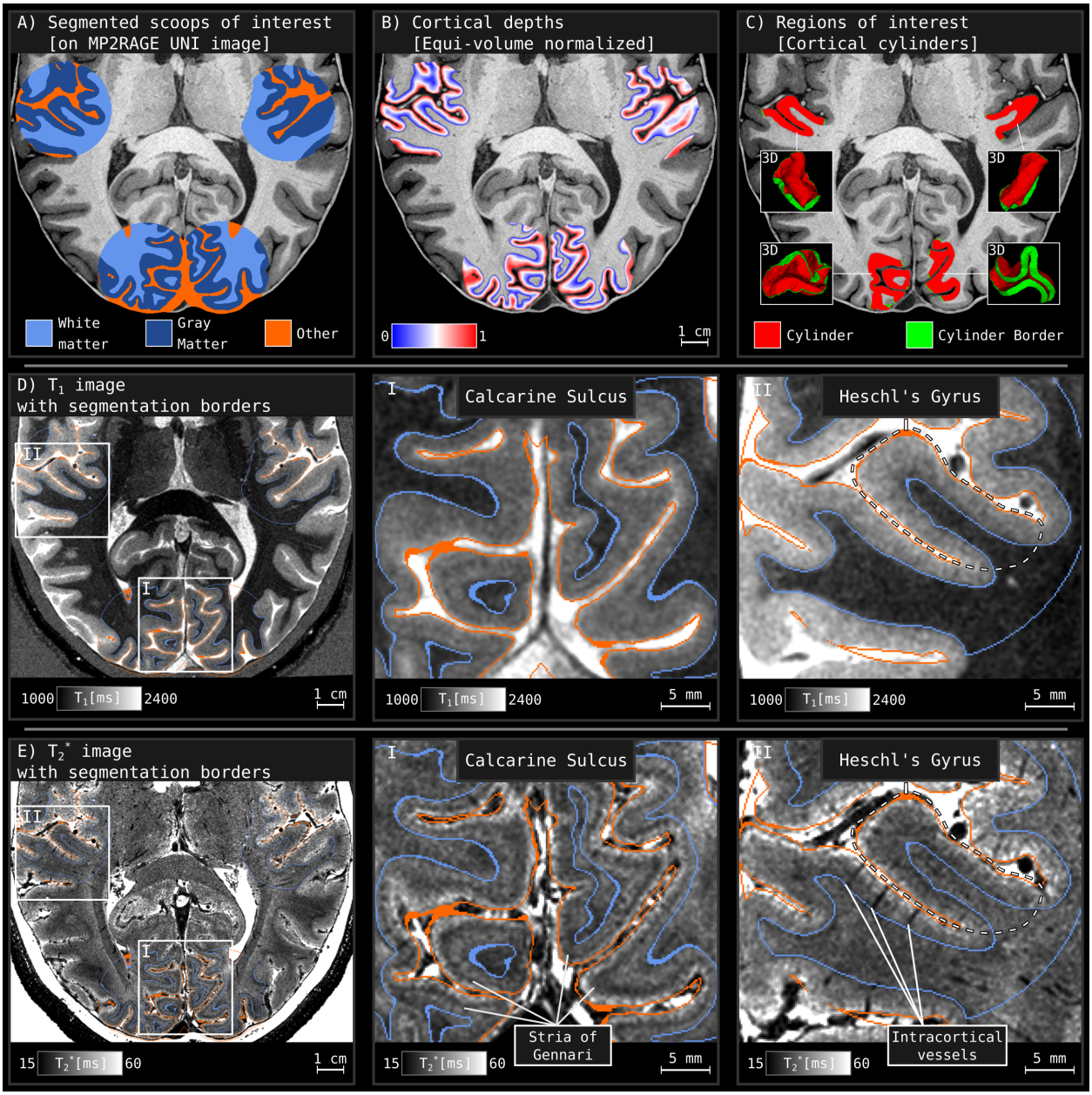

Figure 2: Segmentation, cortical depths, and regions of interest identified for an example subject (sub-04). (A–C) Major processing steps for characterizing our cortical regions of interest. The cortical cylinders in C were geodesically centered at the calcarine sulci and Heschl's gyri anatomical landmarks based on the middle gray-matter voxels. Careful manual tissue segmentation was performed, enabling extraction of gray-matter boundaries and cortical surface topology. **(D–E)** T_1 and T_2^* measurements in the regions of interest with overlaid gray-matter boundaries. Notice that the quality of the T_2^* image allows visualization of fine-scale cortical substructures such as the Stria of Gennari and intracortical vessels in the zoomed-in panels **I-II**. Detailed images of the other participants can be seen in **Supplementary Figure 2**.

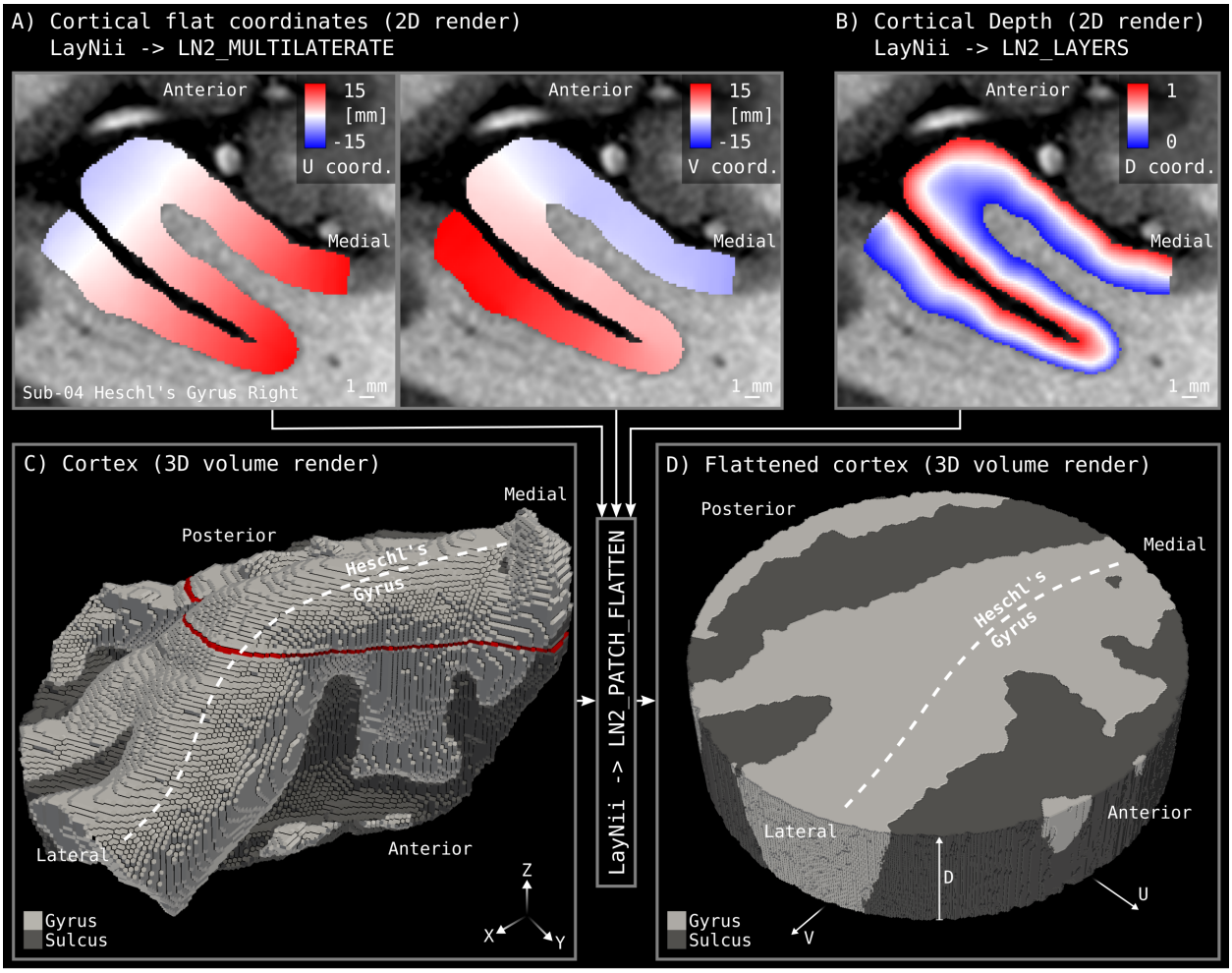

Figure 3: 3D to 3D cortical flattening. Cortical cylinders in the form of *virtual Petri dishes* are used for flattening our regions of interest. A cylinder is centered at our anatomical landmarks and its radius is set to 15 mm. The cylinder height covers the whole cortical thickness. **(A)** Cortical flat coordinates visualized for a 2D slice. **(B)** Cortical equi-volume depth assignment for the same slice. **(C)** Structure of cortical cylinder in original 3D folded brain space (XYZ coordinates). The red line indicates the location of the 2D slice in panels A and B. **(D)** Structure of cortical cylinder after flattening (UVD coordinates).

3 Results

3.1 Angioarchitectonic information within T_2^* images

Given the high quality of our 0.35 mm T_2^* data, we find that simple inspections reveal clearly visible properties of intracortical vessels. For instance, we are able to visualize penetrating vessel trunks over the cortical surface similar to what is seen with invasive measurement techniques (Duvernoy et al., 1981, Fig. 64). **Figure 4** shows that there are multitude of local T_2^* dips across the cortical surface. While we have manually labeled the most visible dips similar to Duvernoy et al. (1981) in this initial investigation, future studies can improve the detection of such intracortical vessels by developing automatic methods similar to (Bernier et al., 2018; Bollmann et al., 2022; Huck et al., 2019). Following Duvernoy's nomenclature, we call these "intracortical vessels". These intracortical vessels most likely belong to groups 4 and 5 of the "intracortical veins". Unsurprisingly, the labeled intracortical veins in our images often penetrate through the majority of the cortical thickness. Examples of intracortical veins can be observed in the original 3D folded brain space in **Figure 2E** and **Supplementary Figure 2**.

Browsing superficial gray matter reveals large differences between T_2^* measurements due to the presence of pial vessels that lie above the cortex. **Figure 5A** shows such pial vessel effects sampled from the superficial depth in and around

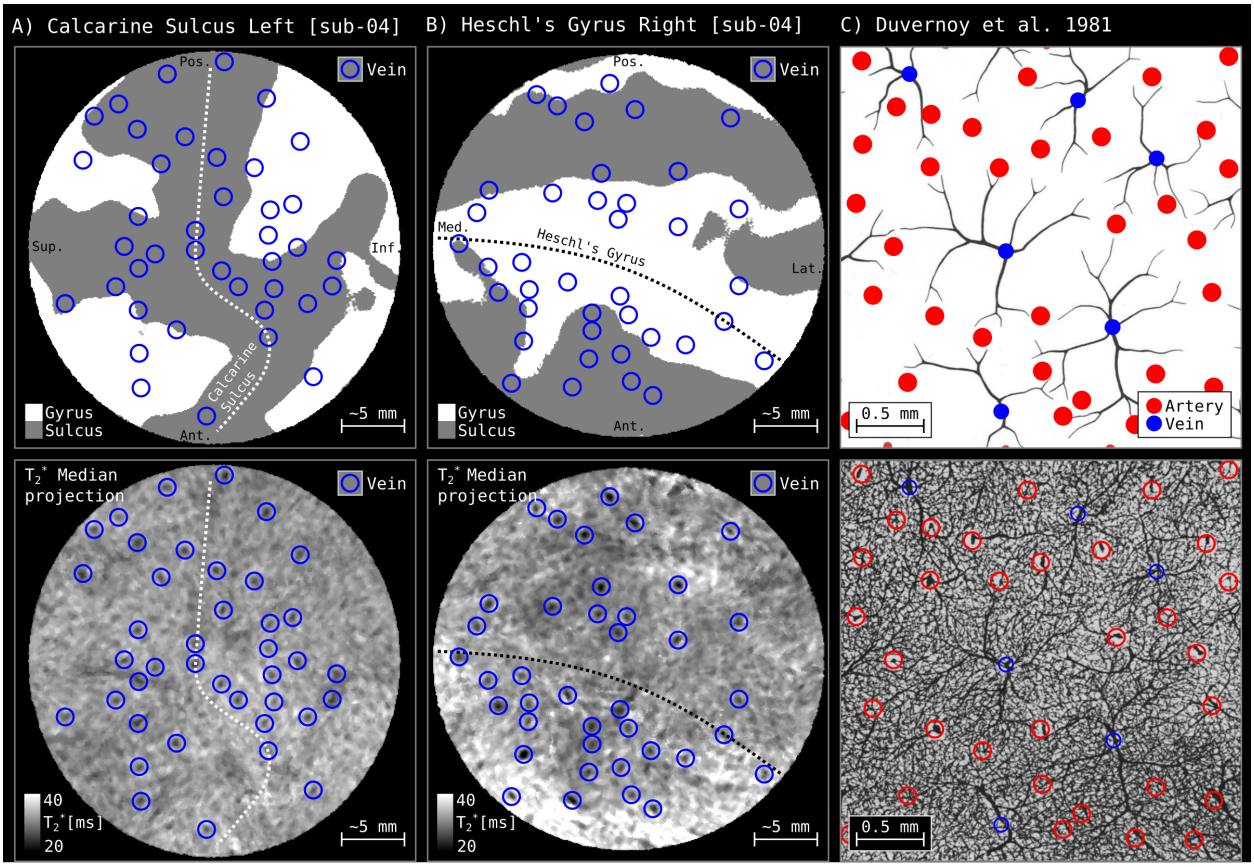

Figure 4: Comparison between in vivo flattened cortical surface representation of T_2^* measurements and ink-gelatin perfusion images from Duvernoy et al. (1981). (A–B) Curvature (top) and median-projected T_2^* measurements (bottom) for two example cortical patches. Median projection is performed to summarize all cortical depths into a single image. **(C)** Manually labeled schematic (top) and original ink injection images (bottom) for a sample patch of tissue as reproduced from Duvernoy et al. (1981).

the calcarine sulcus. Branching impressions of the pial vessels can easily be seen as contiguous low T_2^* regions. This might be due to the deoxyhemoglobin in the vessels affecting the T_2^* signal outside of their trunks (Bause et al., 2020). In addition, **Figure 5B-C** cross-sections reveal the extent of T_2^* darkening can be up to approximately a quarter of the cortical depth. In addition, a few large penetrating intracortical vessels are clearly visible in these cross sections as well.

Aside from the very dark T_2^* vascular impressions on the superficial depths and vertical tubes that travel through the cortical thickness, laminar structures are also visible as horizontal bands in **Figure 5B-C**. For instance the stria of Gennari (Fulton, 1937; Gennari, 1782; Glickstein & Rizzolatti, 1984) is visible as T_2^* darkening around the middle of the cortical thickness of the visual cortex. However, we refrain from attributing this laminar structure only to neuronal layers because Duvernoy et al. (1981) and Pfeifer (1940) showed that there are angioarchitectonic layers within the cortex as well.

3.2 Cortical measurements of T_2^* at 7 T

Our primary focus was to acquire cortical T_2^* measurements that are valuable for optimizing and interpreting several MRI sequences such as T_2^* -weighted anatomical or functional imaging (Cohen-Adad et al., 2012; Deistung et al., 2013; Markuerkiaga et al., 2021; Marques et al., 2017). For instance, high-resolution fMRI studies make use of the T_2^* values across cortical depths to model unwanted vein effects. Therefore, 0.35 mm iso. resolution of our in vivo quantitative imaging dataset is valuable. In addition, optimal T_2^* -weighting parameters are known to vary across brain regions, and previously reported gray matter T_2^* values are biased towards the occipital cortex (Peters et al., 2007). Therefore, to built a quantitative basis for further optimization and interpretation of the MRI signal, we report T_2^* values across cortical depths for both the visual and auditory areas.

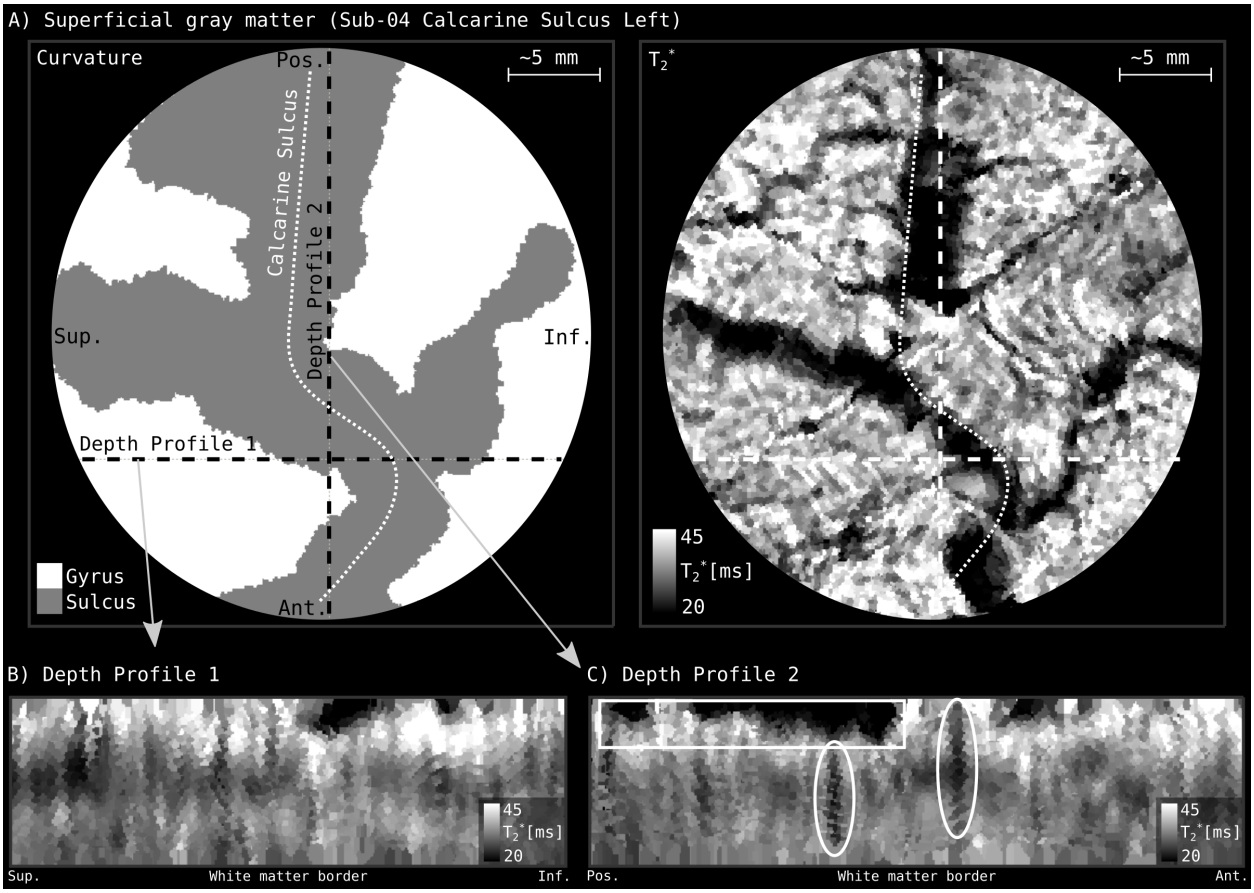

Figure 5: Comparison of flattened T_2^* and T_1 measurements in a single subject (sub-04). (A) Measurements across the cortical surface at the superficial cortical depth. The color associated with each pixel in these images come from exactly one folded brain voxel (processed at 0.175 mm isotropic resolution). T_2^* effects of the pial vessels can be seen as dark impressions in the middle image. **(B–C)**, Measurements for two different cross-sections of cortex. Laminar variations, pial vessel effects (rectangles), and intracortical veins (ellipses) are all visible.

In **Figure 6**, we plotted single-participant T_2^* values across cortical depths for the calcarine sulci and Heschl's gyri in both hemispheres. It can be seen that there is a T_2^* dip at the middle depth of the gray matter in the calcarine sulci, while a similar dip is not visible for Heschl's gyri. This observation follows what is visible to the naked eye in **Figure 2E**, namely there is a layer of low T_2^* values within the calcarine sulcus (Barbier et al., 2002; Budde et al., 2011; Duyn et al., 2007; Federau & Gallichan, 2016; Fukunaga et al., 2010; Kemper et al., 2018; Sánchez-Panchuelo et al., 2012; Zwanenburg et al., 2011). This observation holds for every participant (see **Supplementary Figure 2**) and is qualitatively consistent across the left and right hemispheres of each participant. It can be said that average T_2^* is biologically perturbed across cortical depths.

Looking at the group results in **Figure 7**, we observe that T_2^* variance increases towards the superficial depths in every participant. This could be due to the increased partial voluming with both pial vessels (which causes low T_2^*) and CSF (which causes high T_2^*) that lie above gray matter, and indicates T_2^* is not only neurobiologically biased but also heteroskedastic across depths. Thus, when modelling cortical MRI signals (Havlicek & Uludag, 2020; Markuerkiaga et al., 2021; Uludag et al., 2009), care must be taken not only to account for varying T_2^* but also accounting for the varying amounts of T_2^* variance across cortical depths. In contrast, when considering the white matter voxels below the gray matter (superficial white matter), variance appears to be similar to the deep gray matter voxels. Overall, we observe slightly reduced T_2^* values in white matter compared to gray matter, which could be attributed to the increased myelin content in white matter as well as increased iron content in U-fibers (Kirilina et al., 2020).

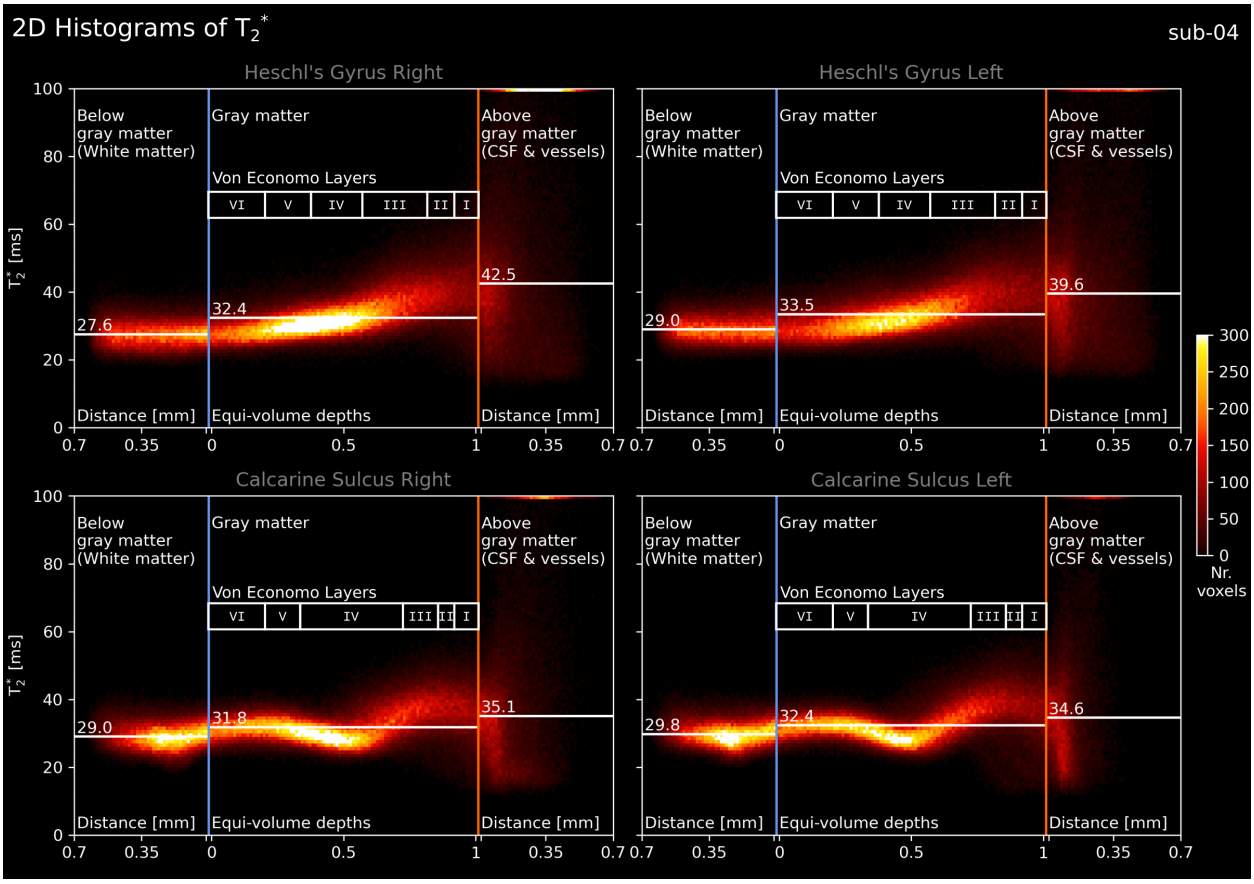

Figure 6: 2D histograms of T_2^* as a function of cortical depth for a single participant (sub-04). The vertical lines show gray matter borders: blue for the inner gray-matter border and orange for the outer gray-matter border (see **Figure 2D-E**). Horizontal white lines show the average T_2^* for different tissue sections: below gray matter, gray matter, and above gray matter. Note the topmost bins within the above gray-matter section showing very high T_2^* voxels that are out of range. See figure supplements showing each individual at `https://osf.io/n5bj7` under *Supplementary Figures* folder.

4 Discussion

In this study, we have demonstrated MRI acquisition and analysis of high-quality mesoscopic anatomical T_2^* data from five living human brains ($0.35 \times 0.35 \times 0.35$ mm^3 resolution). Our freely dataset include quantitative T_2^* measurements from approximately 1/3 of the brain including the primary visual and auditory areas. We provide qualitative demonstrations of fine-scale details captured in our dataset through flat maps. These flat maps reveal clear mesoscopic cortical substructures of the living human brain such as layers and intracortical vessels, and these are discernible without any statistical analysis. We also, for the first time, report quantitative gray matter T_2^* values at 7 Tesla across cortical depths together with superficial white matter, as well as above pial surface measurements for the visual and auditory cortices.

4.1 Mesoscopic Properties Observed in Visual and Auditory Cortices

Our mesoscopic T_2^* images reveal clear cortical substructures. Two main types of cortical substructures are visible: layers and vessels. With regards to the cortical layers, there appears to be a substantial difference between the visual and auditory cortices. In the visual cortex, a distinct layer around the middle gray-matter depth is clearly visible as has been previously shown with in vivo MRI at mesoscopic resolutions (Barbier et al., 2002; Budde et al., 2011; Duyn et al., 2007; Federau & Gallichan, 2016; Fukunaga et al., 2010; Kemper et al., 2018; Lüsebrink et al., 2021; Zwanenburg et al., 2011). This structure is the stria of Gennari (Fulton, 1937; Gennari, 1782; Glickstein & Rizzolatti, 1984). On the other hand, in the auditory cortex, an equally distinct layering was not immediately visible. This is consistent

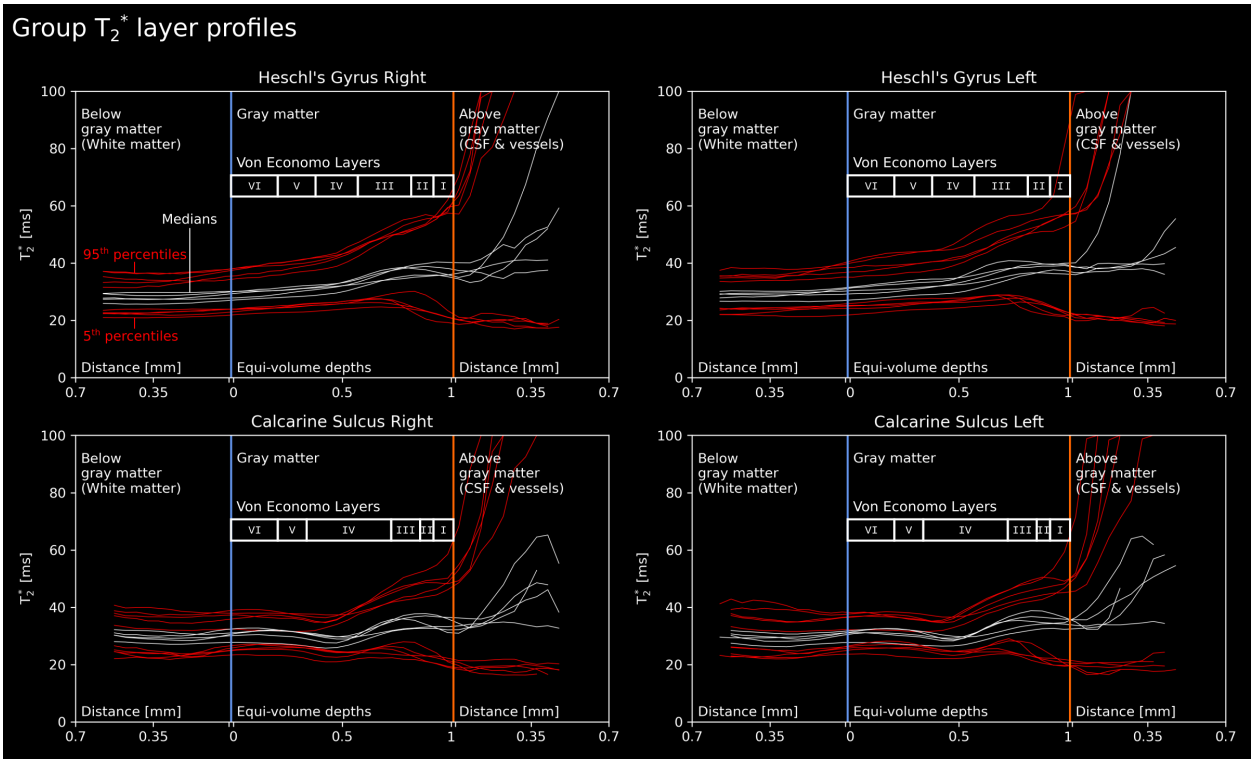

Figure 7: Line plots of T_2^* as a function of cortical depth for all five subjects. Format similar to **Figure 6**. White lines show the median T_2^* calculated for successive bins of cortical depth. Red lines show the 5th & 95th percentiles observed for these bins.

with post-mortem imaging studies (Wallace et al., 2016; Wallace et al., 2002) and previous sub-millimeter attempts to identify layers within the auditory cortex (De Martino et al., 2015; Dick et al., 2012; Dick et al., 2017; Wasserthal et al., 2014). The difference between the visual cortex layers and the auditory cortex layers in T_2^* and T_1 images highlight how unique the visual cortex layering is compared to the rest of the cortex. However, as argued within (Kuehn et al., 2017; Skeide et al., 2018; Wallace et al., 2016), mesoscopic in vivo imaging may still be insufficient to capture the subtle changes in myeloarchitecture aside from primary visual cortex where layer IV is extremely thick. Our mesoscopic T_2^* images also show clear presence of vascular structures within the cortex. This is interesting because seminal neuroscience works highlight laminar cytoarchitecture, myeloarchitecture, and fiber architecture (Turner, 2013a, 2013b), but rarely mention laminar angioarchitecture. It has been shown that the angioarchitecture of the cortex exhibits a laminar arrangement both across depths and over the cortical surface (Duvernoy et al., 1981; Pfeifer, 1940). Specifically within Duvernoy's work, four angioarchitectural layers are postulated. When the first two angioarchitectonic layers combined, it can be seen that these layers almost equally divide the human cortex. Given that T_2^* contrast has a substantial contribution from the presence of blood, the laminar patterns we are observing within the visual cortex (see **Figure 2E** and **Supplementary Figure 2**) may also reflect laminar angioarchitecture (also see Koopmans et al. (2011) Fig.6). Indeed, Pfeifer (1940) showed increased density of blood vessels in middle cortical layers, which might be the origin of the T_2^* dip we have observed. More broadly, what constitutes the living brain might be biased by the post-mortem focus within the last century where angioarchitectonic layering within the cortex is partially neglected due to the draining of blood and degradation of blood vessels during fixation and embedding processes. We invite others to make use of our mesoscopic dataset to further study cortical angioarchitecture.

4.2 Challenges That Remain for Mesoscopic Imaging

There are several remaining challenges for in vivo mesoscopic MRI. The most obvious challenge is head motion (Jezzard & Clare, 1999; Zaitsev et al., 2015). In our study, all participants were highly experienced for being scanned and were able to keep their heads relatively still within the data acquisition periods. In addition, we used 3D acquisition sequences rather than 2D sequences; in 3D sequences, within-run head motion is more forgiving. Another advantage of 3D sequences is that they generally enable higher resolution and SNR (Poser et al., 2010; Stirnberg et al., 2017). As a result of using 3D acquisitions and experienced participants, we achieved highly detailed images of cortical

substructures, even those as small as intracortical vessels. This result shows that mesoscopic MRI is practical when head motion is minimized and when using 3D acquisition sequences with sufficient SNR, participant preselection. However, it would be critical to use additional strategies to minimize head motion of less experienced participants, such as prospective motion correction (Lüsebrink et al., 2017; Maclaren et al., 2012; Mattern et al., 2018; Stucht et al., 2015; Zaitsev et al., 2017), 3D fat-based motion navigators (Federau & Gallichan, 2016; Gallichan et al., 2016; Gretsch et al., 2020), 3D printed head casts (Power et al., 2019), and field monitoring (Barmet et al., 2008; Eschelbach et al., 2019). We think that more advanced head motion minimization methods have potential to yield crisper mesoscopic images and broaden the application of mesoscopic MRI to a larger audience. While we fully acknowledge that we performed retrospective head motion correction rather than prospective motion correction (see **Supplementary Table 1**), we believe that our results make a good argument for the importance of participant selection when prospective motion correction methods are inaccessible (see **Supplementary Figure 2. 3, 4**). We have consistently collected high quality data by combining pre-selection of experienced participants with shorter "fMRI-style" (maximum 10-15 min.) acquisition durations that allow for resting in-between runs.

In our study, we used conservative amounts of image acquisition acceleration. This resulted in somewhat lengthy but still feasible anatomical acquisition durations (10–15 min). The choice of minimal acceleration was deliberate in order to minimize artifacts, maximize SNR, and thereby establish a benchmark dataset. However, a persistent challenge for mesoscopic imaging is long data acquisition times. Faster acquisitions leveraging e.g. echo planar imaging (Sanchez Panchuelo et al., 2021b) are especially needed for clinical populations. From a methods development perspective, our densely sampled high-resolution multi-echo dataset might be useful for efforts in which a dataset is subsampled and methods are developed to optimally recover the full dataset from limited data, such as parallel imaging or model based reconstructions (Ye, 2019).

Even in an ideal case of no head motion, in vivo MRI presents a unique challenge, namely, effects due to the motion of blood. Especially within large arteries, blood reaches very high speeds (Rahman Rasyada & Azhim, 2018). Such moving blood is known to cause imaging artifacts (Larson et al., 1990; Wehrli, 1990), especially when the time between the phase-encoding and readout (frequency encoding) stages of the MRI signal acquisition gets longer. An obvious case where blood motion artifacts are visible is multi-echo acquisition, where each phase-encoded line of k-space is measured using several successive readouts to acquire multiple echos. Our ME GRE images have captured this artifact in unprecedented detail (**Supplementary Figure 1**). Importantly, this artifact is not specific to our anatomical multi-echo acquisition. Any MRI sequence that has long (> 4 ms) time difference between the phase-encoding and readout stages is bound to have this artifact, given that the arterial signal is not effectively nulled. Especially in echo planar imaging (EPI) readouts (Bernstein et al., 2004) commonly used for fMRI, where the image is acquired within very long readout durations (e.g. > 30 ms), this blood motion artifact will strongly exhibit itself. Fortunately, the blood motion artifact is limited to regions near large arteries (> 1 mm diameter). However, studies that rely on accurate and precise quantification of the brain tissue (e.g. see literature within Mancini et al., 2020), such as multi-parametric mapping and in vivo histology (Edwards et al., 2018) should be aware of this artifact. In addition, studies that rely on weighted contrasts, such as T_2^* -weighted, should be cautious of this artifact because the arterial signal can be smeared towards the gray matter, causing artifactually hyperintense regions. Moreover, the artifact may corrupt contrast locally by introducing dark regions in the actual position of an artery as its signal is displaced away from its trunk. This can cause arteries to appear similar to the venous signal in T_2^* -weighted images. Thus, dark regions in T_2^* -weighted images - especially near the pial surface - cannot be conclusively labeled as veins, as has been suggested (Kay et al., 2019; Moerel et al., 2018; Olman et al., 2007).

4.3 Future Neuroscience Applications for Mesoscopic MRI

Our study suggests exciting possibilities for mesoscopic imaging. From a clinical perspective, mesoscopic in vivo imaging of human cortical architecture creates the opportunity to develop a novel set of biomarkers for the healthy development of adult cortical laminar structure and its disruption in neurological and psychiatric disorders (McColgan et al., 2021). Prime candidate conditions for mesoscopic imaging include well-established but subtle abnormalities in laminar structure that currently lack clear imaging correlates such as layer-specific neuronal loss in amyotrophic lateral sclerosis (Braak et al., 2017) and Huntington's disease (Rüb et al., 2016), as well as developmental disruption of cortical layering in focal cortical dysplasia (Blümcke et al., 2011). From a cortical parcellation perspective, future analyses may investigate whether inter-regional variability in laminar structure can be leveraged for parcellating cortical areas using approaches like those used for cytoarchitectonic data (Dinse et al., 2015; Gulban et al., 2020; Morosan et al., 2001; Schleicher et al., 1999; Zachlod et al., 2020). With additional acquisition time, it is clear that mesoscopic coverage of 1/3 of the brain can be easily increased to include the whole brain by scanning different slabs and stitching them together. From an fMRI perspective, imaging the angioarchitectonic substructure of the cortex is necessary for building biophysical models of the fMRI signal (Akbari et al., 2021; Báez-Yánez et al., 2020; Cheng et al., 2019; Havlicek & Uludag, 2020; Polimeni & Lewis, 2021). The spatial variability of fMRI signals due to mesoscopic angioarchitecture is

not well understood. The effect of intracortical veins has been the focus of fMRI signal modelling so far (Havlicek & Uludag, 2020; Heinzle et al., 2016; Markuerkiaga et al., 2016; Markuerkiaga et al., 2021; Uludag et al., 2009), although empirical studies have shown considerable contributions from pial veins (Bause et al., 2020; Olman et al., 2007; Turner, 2002; Winawer et al., 2010). Further, several sub-millimeter fMRI studies have found heterogeneous response profiles across cortical depths (Chen et al., 2013; Fracasso et al., 2018; Kashyap et al., 2018). Thus, the angioarchitecture information in our mesoscopic images might help extend classical models of fMRI signals to consider the heterogeneity of the underlying vasculature and improve the interpretability of laminar BOLD fMRI profiles.

5 Appendix A

5.1 MP2RAGE T_1 cortical depth profiles

We highlight that our primary focus for acquiring the T_1 contrast was for cortical gray matter segmentation. Therefore, we have used a speed-optimized MP2RAGE sequence that provided good contrasts for cortical segmentation purposes. However, we believe that there could be some value in reporting our findings. T_1 contrast is clearly shown to be related to myelination (Leuze et al., 2017; Morawski et al., 2018) and therefore used for delineating areal borders (Cohen-Adad et al., 2012; Deistung et al., 2013; Dick et al., 2012; Dinse et al., 2015; Haast et al., 2016; Marques et al., 2017; Sanchez Panchuelo et al., 2021b; Sánchez-Panchuelo et al., 2012).

We plot single-subject T_1 measurements across cortical depths for the calcarine sulci and Heschl's gyri in both hemispheres in **Figure A.1**. We observe a dip of T_1 values in middle of the cortical thickness in the calcarine sulci, but a similar dip is not visible for Heschl's gyri. This T_1 dip is harder to identify in individual brain images compared to the dip in T_2^* . Looking at the variance of T_1 across cortical depths in group results **Figure A.2**, we find that variance does not increase as drastically as in T_2^* profiles (see **Figure 7**). This suggests that T_1 is less sensitive to laminar architecture than T_2^* . Looking at the above gray-matter voxels, it can be seen that the variance increases, but less than in the T_2^* profiles. This is because vessels show on average similar T_1 to gray matter, while CSF has a higher T_1 (Zhang et al., 2013).

A comparison between T_1 and T_2^* images leads to interesting observations (e.g. **Fig.2D-E**). CSF, arteries, and veins can be considered as the three main tissue types that lie above gray matter. When looking at the T_2^* images, vessels can be seen as regions with low T_2^* while CSF has very high T_2^* . In **Figure 2D-E**, looking at the low T_2^* voxels in T_1 images reveal that large (> 1 mm diameter) arteries and veins seem to have very different T_1 values. This difference might be due to the higher velocity of the blood in the arteries compared to veins affecting proper inversion of the arterial signal during MP2RAGE acquisition. However, aside from the arteries, it can be seen that most of the low T_2^* voxels above gray matter are not visible in MP2RAGE T_1 images. This observation is interesting because it shows that T_2^* contrast, which is sensitive to macromolecular content and iron, is highly advantageous for localizing veins compared to T_1 contrast, which is mostly sensitive to the macromolecular content.

Another interesting yet subtle detail is the consistent asymmetry between the average gray matter T_1 values across hemispheres. It can be seen that the right hemisphere average gray matter T_1 is higher in all participants compared to their left hemisphere when comparing Heschl's gyri. Such asymmetry is not visible when comparing the calcarine sulci. Given the calcarine sulci ROIs are much closer in space compared to Heschl's gyri ROIs, we attribute this average gray matter T_1 difference to residual the transmit field inhomogeneities based on Marques and Gruetter (2013).

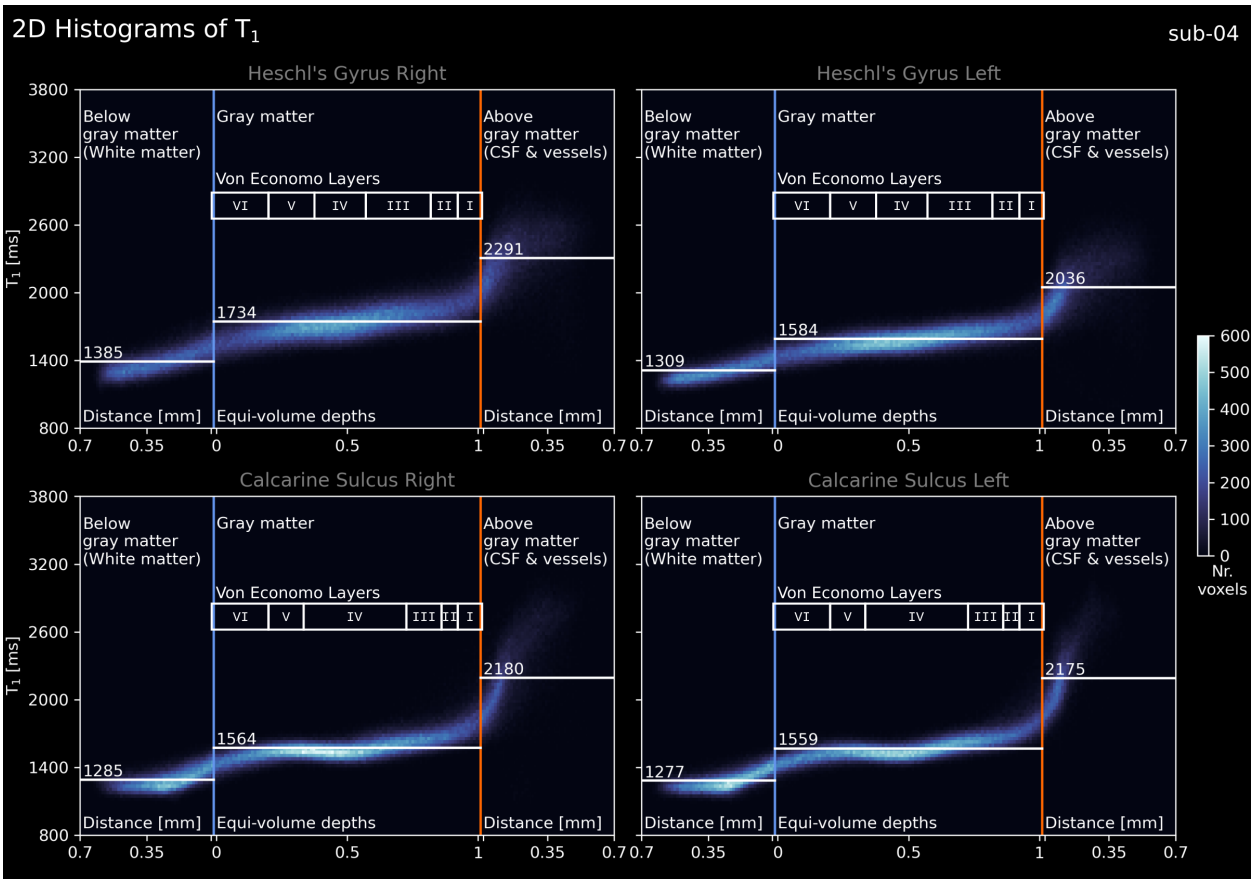

Figure A. 1: 2D histograms of T_1 as a function of cortical depth for a single subject (sub-04). The vertical lines show the gray-matter borders: blue for the inner gray-matter border and orange for the outer gray-matter border (see **Figure 2D-E**). Horizontal white lines show the median T_1 for different tissues: below gray matter, gray matter, and above gray matter. See figure supplements showing each individual at `https://osf.io/n5bj7` under *Supplementary Figures* folder.

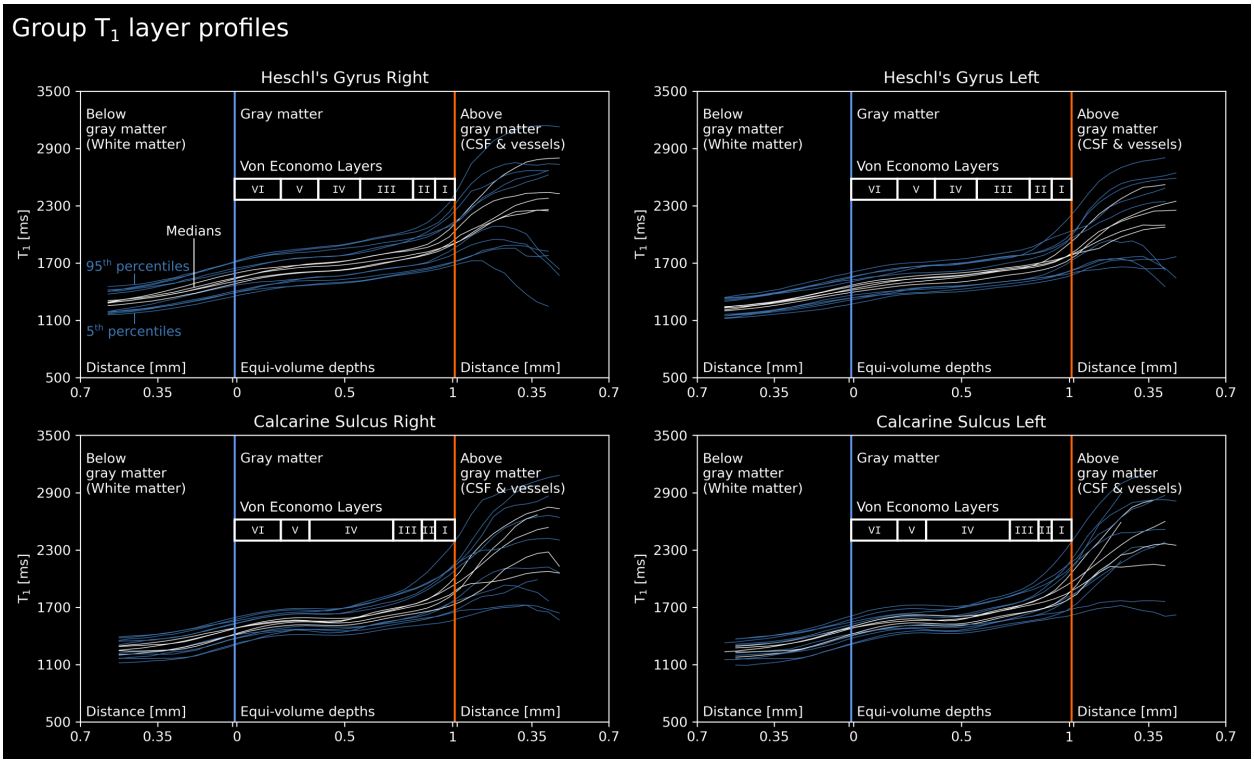

Figure A. 2: Line plots of T_1 as a function of cortical depth for all five subjects. Format similar to **Fig.A.1**. White lines show the median T_1 calculated for successive bins of cortical depth. Blue lines show 5th & 95th percentiles observed for these bins.

Author Contributions

According to the CRediT (Contributor Roles Taxonomy) system.

Conceptualization: O.F.G., D.I.
Data curation: O.F.G., D.I.
Formal Analysis: O.F.G.
Funding acquisition: D.I., R.G.
Investigation: O.F.G., D.I.
Methodology: O.F.G., D.I., K.K., S.B., R.H.
Project administration: O.F.G., D.I., K.K.
Resources: O.F.G., R.G., R.H., B.A.P.
Software: O.F.G., R.H.
Supervision: O.F.G., D.I., K.K.
Validation: O.F.G., D.I., K.W., S.B.
Visualization: O.F.G., K.K., D.I.
Writing – original draft: O.F.G., D.I., K.K.
Writing – review & editing: O.F.G., D.I., K.K., S.B., K.W., R.H., B.A.P., R.G.

Acknowledgements

We thank Jeff Duyn, Nikola Stikov, Jonathan Polimeni, David Norris, and Robert Turner for their comments on the first version of our preprint, we have benefited from these valuable comments to improve our manuscript. We thank Federico De Martino for his contributions in the early stages of this study. We thank Valentin Kemper, Martin Havlicek, Kamil Uludag, Nikolaus Weiskopf, Logan Dowdle, Jonathan Winawer, Simon Robinson, Korbinian Eckstein, Michelle Moerel for fruitful discussions at various stages of this project. Additionally, we thank Elizabeth DuPre, Gilles De Hollander, Taylor Salo, and Agah Karakuzu for their help with Brain Imaging Data Structure (BIDS) organization of our dataset (https://neurostars.org/t/multi-echo-anatomical-mri-bids-questions/17157).

SB was funded from the NHMRC-NIH BRAIN Initiative Collaborative Research Grant APP1117020, and NIH grant 1R01MH111419. R.H. was funded from the NWO VENI project 016.Veni.198.032. K.W. was funded by the Wellcome Trust (215901/Z/19/Z). B.P. was partially funded by the NWO VIDI grant 16.Vidi.178.052, by the National Institute for Health grant R01MH/111444 (PI: David Feinberg) and by the H2020 FET-Open AROMA grant agreement no. 88587. R.G. received funding from the European Union's Horizon 2020 Framework Programme for Research and Innovation under the Specific Grant Agreement No. 945539 (Human Brain Project SGA3). O.F.G. and R.G. have financial interest tied to Brain Innovation. Scanning was supported by FPN (faculty of psychology and neuroscience) via the MBIC grant scheme. Scanning was performed at the facilities of Scannexus B.V. (Maastricht, Netherlands). T_2^* -mapping was done with an ASPIRE sequence, kindly provided by Simon Robinson via SIEMENS C2P.

References

Akbari, A., Bollmann, S., Ali, T. S., & Barth, M. (2021). Modelling the depth-dependent VASO and BOLD responses in human primary visual cortex. *bioRxiv*, 1–31.

Allen, E. J., St-Yves, G., Wu, Y., Breedlove, J. L., Prince, J. S., Dowdle, L. T., Nau, M., Caron, B., Pestilli, F., Charest, I., Hutchinson, J. B., Naselaris, T., & Kay, K. (2022). A massive 7T fMRI dataset to bridge cognitive neuroscience and artificial intelligence. *Nature Neuroscience*, *25*(1), 116–126. https://doi.org/10.1038/s41593-021-00962-x

Báez-Yánez, M. G., Siero, J. C., & Petridou, N. (2020). A statistical 3D model of the human cortical vasculature to compute the hemodynamic fingerprint of the BOLD fMRI signal. *bioRxiv*, *31*(0), 1–63.

Barbier, E. L., Marrett, S., Danek, A., Vortmeyer, A., Van Gelderen, P., Duyn, J., Bandettini, P., Grafman, J., & Koretsky, A. P. (2002). Imaging cortical anatomy by high-resolution MR at 3.0T: Detection of the stripe of Gennari in visual area 17. *Magnetic Resonance in Medicine*, *48*(4), 735–738. https://doi.org/10.1002/mrm.10255

Barmet, C., De Zanche, N., & Pruessmann, K. P. (2008). Spatiotemporal magnetic field monitoring for MR. *Magnetic Resonance in Medicine*, *60*(1), 187–197. https://doi.org/10.1002/mrm.21603

Bause, J., Polimeni, J. R., Stelzer, J., In, M. H., Ehses, P., Kraemer-Fernandez, P., Aghaeifar, A., Lacosse, E., Pohmann, R., & Scheffler, K. (2020). Impact of prospective motion correction, distortion correction methods and large vein bias on the spatial accuracy of cortical laminar fMRI at 9.4 Tesla. *NeuroImage*, *208*(April 2019). https://doi.org/10.1016/j.neuroimage.2019.116434

Bazin, P.-L., Weiss, M., Dinse, J., Schäfer, A., Trampel, R., & Turner, R. (2014). A computational framework for ultra-high resolution cortical segmentation at 7Tesla. *NeuroImage*, *93 Pt 2*, 201–9. https://doi.org/10.1016/j.neuroimage.2013.03.077

Bentivoglio, M., & Mazzarello, P. (2009). Chapter 12 The anatomical foundations of clinical neurology. *Handbook of clinical neurology* (pp. 149–168). Elsevier. https://doi.org/10.1016/S0072-9752(08)02112-X

Bernier, M., Cunnane, S. C., & Whittingstall, K. (2018). The morphology of the human cerebrovascular system. *Human Brain Mapping*, *39*(12), 4962–4975. https://doi.org/10.1002/hbm.24337

Bernstein, M. A., King, K. F., & Zhou, X. J. (2004). *Handbook of MRI Pulse Sequences*. Elsevier. https://doi.org/10.1016/B978-0-12-092861-3.X5000-6

Blümcke, I., Thom, M., Aronica, E., Armstrong, D. D., Vinters, H. V., Palmini, A., Jacques, T. S., Avanzini, G., Barkovich, A. J., Battaglia, G., Becker, A., Cepeda, C., Cendes, F., Colombo, N., Crino, P., Cross, J. H., Delalande, O., Dubeau, F., Duncan, J., … Spreafico, R. (2011). The clinicopathologic spectrum of focal cortical dysplasias: a consensus classification proposed by an ad hoc Task Force of the ILAE Diagnostic Methods Commission. *Epilepsia*, *52*(1), 158–74. https://doi.org/10.1111/j.1528-1167.2010.02777.x

Bok, S. T. (1959). *Histonomy of the Cerebral Cortex*. Elsevier.

Bollmann, S., Mattern, H., Bernier, M., Robinson, S. D., Park, D., Speck, O., & Polimeni, J. R. (2022). Imaging of the pial arterial vasculature of the human brain in vivo using high-resolution 7T time-of-flight angiography. *eLife*, *11*, 2021.06.09.447807. https://doi.org/10.7554/eLife.71186

Braak, H., Ludolph, A. C., Neumann, M., Ravits, J., & Del Tredici, K. (2017). Pathological TDP-43 changes in Betz cells differ from those in bulbar and spinal α-motoneurons in sporadic amyotrophic lateral sclerosis. *Acta neuropathologica*, *133*(1), 79–90. https://doi.org/10.1007/s00401-016-1633-2

Brett, M., Hanke, M., Côté, M.-A., Markiewicz, C., Ghosh, S., Wassermann, D., Gerhard, S., Larson, E., Lee, G. R., Halchenko, Y., Kastman, E., M, C., Morency, F. C., Maloney, B., Rokem, A., Cottaar, M., Millman, J., jaeilepp, Gramfort, A., … Nimmo-Smith, I. (2017). nipy/nibabel: 2.2.0. https://doi.org/10.5281/zenodo.1011207

Bridge, H., Clare, S., Jenkinson, M., Jezzard, P., Parker, A. J., & Matthews, P. M. (2005). Independent anatomical and functional measures of the V1/V2 boundary in human visual cortex. *Journal of Vision*, *5*(2), 93–102. https://doi.org/10.1167/5.2.1

Brinkmann, R. (2008). *The Art and Science of Digital Compositing*. Elsevier. https://doi.org/10.1016/B978-0-12-370638-6.X0001-6

Budde, J., Shajan, G., Hoffmann, J., Uğurbil, K., & Pohmann, R. (2011). Human imaging at 9.4 T using T2*-, phase-, and susceptibility-weighted contrast. *Magnetic Resonance in Medicine*, *65*(2), 544–550. https://doi.org/10.1002/mrm.22632

Chen, H., Zhang, T., Guo, L., Li, K., Yu, X., Li, L., Hu, X., Han, J., Hu, X., & Liu, T. (2013). Coevolution of gyral folding and structural connection patterns in primate brains. *Cerebral cortex (New York, N.Y. : 1991)*, *23*(5), 1208–17. https://doi.org/10.1093/cercor/bhs113

Cheng, X., Berman, A. J., Polimeni, J. R., Buxton, R. B., Gagnon, L., Devor, A., Sakadžić, S., & Boas, D. A. (2019). Dependence of the MR signal on the magnetic susceptibility of blood studied with models based on real microvascular networks. *Magnetic Resonance in Medicine*, *81*(6), 3865–3874. https://doi.org/10.1002/mrm.27660

Cohen-Adad, J. (2014). What can we learn from T2* maps of the cortex? *NeuroImage*, *93 Pt 2*, 189–200. https://doi.org/10.1016/j.neuroimage.2013.01.023

Cohen-Adad, J., Polimeni, J. R., Helmer, K. G., Benner, T., McNab, J. A., Wald, L. L., Rosen, B. R., & Mainero, C. (2012). T 2* mapping and B 0 orientation-dependence at 7T reveal cyto- and myeloarchitecture organization of the human cortex. *NeuroImage*, *60*(2), 1006–1014. https://doi.org/10.1016/j.neuroimage.2012.01.053

De Martino, F., Moerel, M., Xu, J., van de Moortele, P.-F., Ugurbil, K., Goebel, R., Yacoub, E., & Formisano, E. (2015). High-Resolution Mapping of Myeloarchitecture In Vivo: Localization of Auditory Areas in the Human Brain. *Cerebral cortex (New York, N.Y. : 1991)*, *25*(10), 3394–405. https://doi.org/10.1093/cercor/bhu150

Deistung, A., Schäfer, A., Schweser, F., Biedermann, U., Turner, R., & Reichenbach, J. R. (2013). Toward in vivo histology: a comparison of quantitative susceptibility mapping (QSM) with magnitude-, phase-, and R2*-imaging at ultra-high magnetic field strength. *NeuroImage*, *65*, 299–314. https://doi.org/10.1016/j.neuroimage.2012.09.055

Dick, F., Tierney, A. T., Lutti, A., Josephs, O., Sereno, M. I., & Weiskopf, N. (2012). In vivo functional and myeloarchitectonic mapping of human primary auditory areas. *The Journal of neuroscience : the official journal of the Society for Neuroscience*, *32*(46), 16095–105. https://doi.org/10.1523/JNEUROSCI.1712-12.2012

Dick, F. K., Lehet, M. I., Callaghan, M. F., Keller, T. A., Sereno, M. I., & Holt, L. L. (2017). Extensive Tonotopic Mapping across Auditory Cortex Is Recapitulated by Spectrally Directed Attention and Systematically Related to Cortical Myeloarchitecture. *The Journal of neuroscience : the official journal of the Society for Neuroscience*, *37*(50), 12187–12201. https://doi.org/10.1523/JNEUROSCI.1436-17.2017

Dinse, J., Härtwich, N., Waehnert, M. D., Tardif, C. L., Schäfer, A., Geyer, S., Preim, B., Turner, R., & Bazin, P.-L. (2015). A cytoarchitecture-driven myelin model reveals area-specific signatures in human primary and secondary areas using ultra-high resolution in-vivo brain MRI. *NeuroImage*, *114*, 71–87. https://doi.org/10.1016/j.neuroimage.2015.04.023

Duvernoy, H. M., Delon, S., & Vannson, J. L. (1981). Cortical blood vessels of the human brain. *Brain research bulletin*, *7*(5), 519–79. https://doi.org/10.1016/0361-9230(81)90007-1

Duyn, J. H., van Gelderen, P., Li, T.-Q., de Zwart, J. A., Koretsky, A. P., & Fukunaga, M. (2007). High-field MRI of brain cortical substructure based on signal phase. *Proceedings of the National Academy of Sciences*, *104*(28), 11796–11801. https://doi.org/10.1073/pnas.0610821104

Eckstein, K., Dymerska, B., Bachrata, B., Bogner, W., Poljanc, K., Trattnig, S., & Robinson, S. D. (2018). Computationally Efficient Combination of Multi-channel Phase Data From Multi-echo Acquisitions (ASPIRE). *Magnetic resonance in medicine*, *79*(6), 2996–3006. https://doi.org/10.1002/mrm.26963

Edwards, L. J., Kirilina, E., Mohammadi, S., & Weiskopf, N. (2018). Microstructural imaging of human neocortex in vivo. *NeuroImage*, *182*, 184–206. https://doi.org/10.1016/j.neuroimage.2018.02.055

Eschelbach, M., Aghaeifar, A., Bause, J., Handwerker, J., Anders, J., Engel, E.-M., Thielscher, A., & Scheffler, K. (2019). Comparison of prospective head motion correction with NMR field probes and an optical tracking system. *Magnetic Resonance in Medicine*, *81*(1), 719–729. https://doi.org/10.1002/mrm.27343

Federau, C., & Gallichan, D. (2016). Motion-correction enabled ultra-high resolution in-vivo 7T-MRI of the brain. *PLoS ONE*, *11*(5), 1–12. https://doi.org/10.1371/journal.pone.0154974

Finger, S., Boller, F., & Tyler, K. (2009). *Handbook of Clinical Neurology HIstory of Neurology* (Vol. 95). Elsevier.

Fracasso, A., Luijten, P. R., Dumoulin, S. O., & Petridou, N. (2018). Laminar imaging of positive and negative BOLD in human visual cortex at 7 T. *NeuroImage*, *164*(February 2017), 100–111. https://doi.org/10.1016/j.neuroimage.2017.02.038

Fracasso, A., Petridou, N., & Dumoulin, S. O. (2016). Systematic variation of population receptive field properties across cortical depth in human visual cortex. *NeuroImage*, *139*, 427–438. https://doi.org/10.1016/j.neuroimage.2016.06.048

Fukunaga, M., Li, T. Q., Van Gelderen, P., De Zwart, J. A., Shmueli, K., Yao, B., Lee, J., Maric, D., Aronova, M. A., Zhang, G., Leapman, R. D., Schenck, J. F., Merkle, H., & Duyn, J. H. (2010). Layer-specific variation of iron content in cerebral cortex as a source of MRI contrast. *Proceedings of the National Academy of Sciences of the United States of America*, *107*(8), 3834–3839. https://doi.org/10.1073/pnas.0911177107

Fulton, J. F. (1937). A Note on Francesco Gennari and the Early History of Cytoarchitectural Studies of the Cerebral Cortex. *Bulletin of the Institute of the History of Medicine*, *5*(10), 895–913.

Gallichan, D., Marques, J. P., & Gruetter, R. (2016). Retrospective correction of involuntary microscopic head movement using highly accelerated fat image navigators (3D FatNavs) at 7T. *Magnetic Resonance in Medicine*, *75*(3), 1030–1039. https://doi.org/10.1002/mrm.25670

Gennari, F. (1782). De Peculiari Structura Cerebri. Nonnullisque ejus morbis. *Ex Regio Typographeo, Parma.*, *44*(0).

Geyer, S. (2013). *Microstructural Parcellation of the Human Cerebral Cortex* (S. Geyer & R. Turner, Eds.). Springer Berlin Heidelberg. https://doi.org/10.1007/978-3-662-45766-5

Glickstein, M., & Rizzolatti, G. (1984). Francesco Gennari and the structure of the cerebral cortex. *Trends in Neurosciences*, *7*(12), 464–467. https://doi.org/10.1016/S0166-2236(84)80255-6

Gretsch, F., Mattern, H., Gallichan, D., & Speck, O. (2020). Fat navigators and Moiré phase tracking comparison for motion estimation and retrospective correction. *Magnetic Resonance in Medicine*, *83*(1), 83–93. https://doi.org/10.1002/mrm.27908

Gulban, O. F., Goebel, R., Moerel, M., Zachlod, D., Mohlberg, H., Amunts, K., & De Martino, F. (2020). Improving a probabilistic cytoarchitectonic atlas of auditory cortex using a novel method for inter-individual alignment. *eLife*, *9*, 1–29. https://doi.org/10.7554/eLife.56963

Gulban, O. F., Schneider, M., Marquardt, I., Haast, R. A. M., & De Martino, F. (2018). A scalable method to improve gray matter segmentation at ultra high field MRI. *PloS one*, *13*(6), e0198335. https://doi.org/10.1371/journal.pone.0198335

Haast, R. A. M., Ivanov, D., Formisano, E., & Uludağ, K. (2016). Reproducibility and Reliability of Quantitative and Weighted T1 and T2* Mapping for Myelin-Based Cortical Parcellation at 7 Tesla. *Frontiers in neuroanatomy*, *10*(NOV), 112. https://doi.org/10.3389/fnana.2016.00112

Havlicek, M., & Uludag, K. (2020). A dynamical model of the laminar BOLD response. *NeuroImage*, 116209. https://doi.org/10.1016/j.neuroimage.2019.116209

Heinzle, J., Koopmans, P. J., den Ouden, H. E. M., Raman, S., & Stephan, K. E. (2016). A hemodynamic model for layered BOLD signals. *NeuroImage*, *125*, 556–570. https://doi.org/10.1016/j.neuroimage.2015.10.025

Huber, L. ((, Poser, B. A., Bandettini, P. A., Arora, K., Wagstyl, K., Cho, S., Goense, J., Nothnagel, N., Morgan, A. T., van den Hurk, J., Müller, A. K., Reynolds, R. C., Glen, D. R., Goebel, R., & Gulban, O. F. (2021). LayNii: A software suite for layer-fMRI. *NeuroImage*, *237*, 118091. https://doi.org/10.1016/j.neuroimage.2021.118091

Huck, J., Wanner, Y., Fan, A. P., Jäger, A. T., Grahl, S., Schneider, U., Villringer, A., Steele, C. J., Tardif, C. L., Bazin, P. L., & Gauthier, C. J. (2019). High resolution atlas of the venous brain vasculature from 7 T quantitative susceptibility maps. *Brain Structure and Function*, *224*(7), 2467–2485. https://doi.org/10.1007/s00429-019-01919-4

Hunter, J. D. (2007). Matplotlib: A 2D graphics environment. *Computing In Science & Engineering*, *9*(3), 90–95. https://doi.org/10.1109/MCSE.2007.55

Jezzard, P., & Clare, S. (1999). Sources of distortion in functional MRI data. *Human Brain Mapping*, *8*(2-3), 80–85. https://doi.org/10.1002/(SICI)1097-0193(1999)8:2/3<80::AID-HBM2>3.0.CO;2-C

Jones, E., Oliphant, T., Peterson, P., et al. (2001). {SciPy}: Open source scientific tools for {Python}.

Kashyap, S., Ivanov, D., Havlicek, M., Poser, B. A., & Uludag, K. (2018). Impact of acquisition and analysis strategies on cortical depth-dependent fMRI. *NeuroImage*, *168*, 332–344. https://doi.org/10.1016/j.neuroimage.2017.05.022

Kay, K., Jamison, K. W., Vizioli, L., Zhang, R., Margalit, E., & Ugurbil, K. (2019). A critical assessment of data quality and venous effects in sub-millimeter fMRI. *NeuroImage*, *189*(February), 847–869. https://doi.org/10.1016/j.neuroimage.2019.02.006

Kemper, V. G., De Martino, F., Emmerling, T. C., Yacoub, E., & Goebel, R. (2018). High resolution data analysis strategies for mesoscale human functional MRI at 7 and 9.4T. *NeuroImage*, *164*, 48–58. https://doi.org/10.1016/j.neuroimage.2017.03.058

Kirilina, E., Helbling, S., Morawski, M., Pine, K., Reimann, K., Jankuhn, S., Dinse, J., Deistung, A., Reichenbach, J. R., Trampel, R., Geyer, S., Müller, L., Jakubowski, N., Arendt, T., Bazin, P.-L., & Weiskopf, N. (2020). Superficial white matter imaging: Contrast mechanisms and whole-brain in vivo mapping. *Science Advances*, *6*(41), eaaz9281.

Kleinnijenhuis, M. (2014). *Imaging fibres in the brain*. https://doi.org/10.13140/2.1.4788.7689

Koopmans, P. J., Barth, M., Orzada, S., & Norris, D. G. (2011). Multi-echo fMRI of the cortical laminae in humans at 7T. *NeuroImage*, *56*(3), 1276–1285. https://doi.org/10.1016/j.neuroimage.2011.02.042

Kuehn, E., Dinse, J., Jakobsen, E., Long, X., Schäfer, A., Bazin, P. L., Villringer, A., Sereno, M. I., & Margulies, D. S. (2017). Body Topography Parcellates Human Sensory and Motor Cortex. *Cerebral Cortex*, *27*(7), 3790–3805. https://doi.org/10.1093/cercor/bhx026

Larson, T. C., Kelly, W. M., Ehman, R. L., & Wehrli, F. W. (1990). Spatial misregistration of vascular flow during MR imaging of the CNS: cause and clinical significance. *AJR. American journal of roentgenology*, *155*(5), 1117–24. https://doi.org/10.2214/ajr.155.5.2120946

Leuze, C., Aswendt, M., Ferenczi, E., Liu, C. W., Hsueh, B., Goubran, M., Tian, Q., Steinberg, G., Zeineh, M. M., Deisseroth, K., & McNab, J. A. (2017). The separate effects of lipids and proteins on brain MRI contrast revealed through tissue clearing. *NeuroImage*, *156*(December 2016), 412–422. https://doi.org/10.1016/j.neuroimage.2017.04.021

Lüsebrink, F., Mattern, H., Yakupov, R., Acosta-Cabronero, J., Ashtarayeh, M., Oeltze-Jafra, S., & Speck, O. (2021). Comprehensive ultrahigh resolution whole brain in vivo MRI dataset as a human phantom. *Scientific Data*, *8*(1), 1–14. https://doi.org/10.1038/s41597-021-00923-w

Lüsebrink, F., Sciarra, A., Mattern, H., Yakupov, R., & Speck, O. (2017). T1-weighted in vivo human whole brain MRI dataset with an ultrahigh isotropic resolution of 250 μm. *Scientific data*, *4*, 170032. https://doi.org/10.1038/sdata.2017.32

Maclaren, J., Armstrong, B. S., Barrows, R. T., Danishad, K. A., Ernst, T., Foster, C. L., Gumus, K., Herbst, M., Kadashevich, I. Y., Kusik, T. P., Li, Q., Lovell-Smith, C., Prieto, T., Schulze, P., Speck, O., Stucht, D., & Zaitsev, M. (2012). Measurement and Correction of Microscopic Head Motion during Magnetic Resonance Imaging of the Brain. *PLoS ONE*, *7*(11), 3–11. https://doi.org/10.1371/journal.pone.0048088

Mancini, M., Karakuzu, A., Cohen-Adad, J., Cercignani, M., Nichols, T. E., & Stikov, N. (2020). An interactive meta-analysis of MRI biomarkers of Myelin. *eLife*, *9*, 1–23. https://doi.org/10.7554/eLife.61523

Markuerkiaga, I., Barth, M., & Norris, D. G. (2016). A cortical vascular model for examining the specificity of the laminar BOLD signal. *NeuroImage*, *132*, 491–498. https://doi.org/10.1016/j.neuroimage.2016.02.073

Markuerkiaga, I., Marques, J. P., Bains, L. J., & Norris, D. G. (2021). An in-vivo study of BOLD laminar responses as a function of echo time and static magnetic field strength. *Scientific Reports*, *11*(1), 1–13. https://doi.org/10.1038/s41598-021-81249-w

Marques, J. P., & Gruetter, R. (2013). New developments and applications of the MP2RAGE sequence–focusing the contrast and high spatial resolution R1 mapping. (E. Yacoub, Ed.). *PloS one*, *8*(7), e69294. https://doi.org/10.1371/journal.pone.0069294

Marques, J. P., Khabipova, D., & Gruetter, R. (2017). Studying cyto and myeloarchitecture of the human cortex at ultra-high field with quantitative imaging: R1, R2* and magnetic susceptibility. *NeuroImage*, *147*(December 2016), 152–163. https://doi.org/10.1016/j.neuroimage.2016.12.009

Marques, J. P., Kober, T., Krueger, G., van der Zwaag, W., Van de Moortele, P.-F., & Gruetter, R. (2010). MP2RAGE, a self bias-field corrected sequence for improved segmentation and T1-mapping at high field. *NeuroImage*, *49*(2), 1271–81. https://doi.org/10.1016/j.neuroimage.2009.10.002

Mattern, H., Sciarra, A., Lüsebrink, F., Acosta-Cabronero, J., & Speck, O. (2018). Prospective motion correction improves high-resolution quantitative susceptibility mapping at 7T. *Magnetic Resonance in Medicine*, (July), 9–12. https://doi.org/10.1002/mrm.27509

McColgan, P., Helbling, S., Vaculčiaková, L., Pine, K., Wagstyl, K., Attar, F. M., Edwards, L., Papoutsi, M., Wei, Y., Van den Heuvel, M. P., Tabrizi, S. J., Rees, G., & Weiskopf, N. (2021). Relating quantitative 7T MRI across cortical depths to cytoarchitectonics, gene expression and connectomics. *Human Brain Mapping*, (July), 1–14. https://doi.org/10.1002/hbm.25595

Moerel, M., De Martino, F., Kemper, V. G., Schmitter, S., Vu, A. T., Uğurbil, K., Formisano, E., & Yacoub, E. (2018). Sensitivity and specificity considerations for fMRI encoding, decoding, and mapping of auditory cortex at ultra-high field. *NeuroImage*, *164*(March 2017), 18–31. https://doi.org/10.1016/j.neuroimage.2017.03.063

Morawski, M., Kirilina, E., Scherf, N., Jäger, C., Reimann, K., Trampel, R., Gavriilidis, F., Geyer, S., Biedermann, B., Arendt, T., & Weiskopf, N. (2018). Developing 3D microscopy with CLARITY on human brain tissue: Towards a tool for informing and validating MRI-based histology. *NeuroImage*, *182*(May 2017), 417–428. https://doi.org/10.1016/j.neuroimage.2017.11.060

Morosan, P., Rademacher, J., Schleicher, A., Amunts, K., Schormann, T., & Zilles, K. (2001). Human primary auditory cortex: cytoarchitectonic subdivisions and mapping into a spatial reference system. *NeuroImage*, *13*(4), 684–701. https://doi.org/10.1006/nimg.2000.0715

Nieuwenhuys, R. (2013). The myeloarchitectonic studies on the human cerebral cortex of the Vogt-Vogt school, and their significance for the interpretation of functional neuroimaging data. *Brain structure & function*, *218*(2), 303–52. https://doi.org/10.1007/s00429-012-0460-z

Olman, C. A., Inati, S., & Heeger, D. J. (2007). The effect of large veins on spatial localization with GE BOLD at 3 T: Displacement, not blurring. *NeuroImage*, *34*(3), 1126–1135. https://doi.org/10.1016/j.neuroimage.2006.08.045

Peters, A. M., Brookes, M. J., Hoogenraad, F. G., Gowland, P. A., Francis, S. T., Morris, P. G., & Bowtell, R. (2007). T2* measurements in human brain at 1.5, 3 and 7 T. *Magnetic Resonance Imaging*, *25*(6), 748–753. https://doi.org/10.1016/j.mri.2007.02.014

Petridou, N., Wharton, S. J., Lotfipour, A., Gowland, P., & Bowtell, R. (2010). Investigating the effect of blood susceptibility on phase contrast in the human brain. *NeuroImage*, *50*(2), 491–8. https://doi.org/10.1016/j.neuroimage.2009.12.052

Pfeifer, R. A. (1940). *Die angioarchitektonische areale gliederung der grosshirnrinde*. Georg Thieme.

Polimeni, J. R., & Lewis, L. D. (2021). Imaging faster neural dynamics with fast fMRI: a need for updated models of the hemodynamic response. *Progress in Neurobiology*, (October 2020), 102174. https://doi.org/10.1016/j.pneurobio.2021.102174

Poser, B. A., Koopmans, P. J., Witzel, T., Wald, L. L., & Barth, M. (2010). Three dimensional echo-planar imaging at 7 Tesla. *NeuroImage*, *51*(1), 261–6. https://doi.org/10.1016/j.neuroimage.2010.01.108

Power, J. D., Silver, B. M., Silverman, M. R., Ajodan, E. L., Bos, D. J., & Jones, R. M. (2019). Customized head molds reduce motion during resting state fMRI scans. *NeuroImage*, *189*(October 2018), 141–149. https://doi.org/10.1016/j.neuroimage.2019.01.016

Rahman Rasyada, A., & Azhim, A. (2018). Flow Velocity in Common Carotid Artery. *Carotid artery - gender and health [working title]*. IntechOpen. https://doi.org/10.5772/intechopen.80712

Raichle, M. E. (2009a). A brief history of human brain mapping. *Trends in neurosciences*, *32*(2), 118–26. https://doi.org/10.1016/j.tins.2008.11.001

Raichle, M. e. (2009b). Chapter 18 The origins of functional brain imaging in humans. *Handbook of clinical neurology* (pp. 257–268). Elsevier. https://doi.org/10.1016/S0072-9752(08)02118-0

Rüb, U., Seidel, K., Heinsen, H., Vonsattel, J. P., den Dunnen, W. F., & Korf, H. W. (2016). Huntington's disease (HD): the neuropathology of a multisystem neurodegenerative disorder of the human brain. *Brain pathology (Zurich, Switzerland)*, *26*(6), 726–740. https://doi.org/10.1111/bpa.12426

Sanchez Panchuelo, R. M., Mougin, O., Turner, R., & Francis, S. T. (2021a). Quantitative T1 mapping using multi-slice multi-shot inversion recovery EPI. *NeuroImage*, *234*(July 2020), 117976. https://doi.org/10.1016/j.neuroimage.2021.117976

Sanchez Panchuelo, R. M., Mougin, O., Turner, R., & Francis, S. T. (2021b). Quantitative T1 mapping using multi-slice multi-shot inversion recovery EPI. *NeuroImage*, *234*(February), 117976. https://doi.org/10.1016/j.neuroimage.2021.117976

Sánchez-Panchuelo, R. M., Francis, S. T., Schluppeck, D., & Bowtell, R. W. (2012). Correspondence of human visual areas identified using functional and anatomical MRI in vivo at 7 T. *Journal of Magnetic Resonance Imaging*, *35*(2), 287–299. https://doi.org/10.1002/jmri.22822

Schira, M. M., Kassem, S., Barth, M., Isherwood, Z., Smith, K., Shaw, T., & Paxinos, G. (2022). Human Brain Atlas: The Highest Resolution Maps of the Living Human Brain.

Schleicher, A., Amunts, K., Geyer, S., Morosan, P., & Zilles, K. (1999). Observer-independent method for microstructural parcellation of cerebral cortex: A quantitative approach to cytoarchitectonics. *NeuroImage*. https://doi.org/10.1006/nimg.1998.0385

Skeide, M. A., Bazin, P.-L., Trampel, R., Schäfer, A., Männel, C., von Kriegstein, K., & Friederici, A. D. (2018). Hypermyelination of the left auditory cortex in developmental dyslexia. *Neurology*, *90*(6), e492–e497. https://doi.org/10.1212/WNL.0000000000004931

Stahnisch, F. W. (2010). Chapter 11: on the use of animal experimentation in the history of neurology. *Handbook of clinical neurology*, *95*(100), 129–48. https://doi.org/10.1016/S0072-9752(08)02111-8

Stirnberg, R., Huijbers, W., Brenner, D., Poser, B. A., Breteler, M., & Stöcker, T. (2017). Rapid whole-brain resting-state fMRI at 3 T: Efficiency-optimized three-dimensional EPI versus repetition time-matched simultaneous-multi-slice EPI. *NeuroImage*, *163*(August), 81–92. https://doi.org/10.1016/j.neuroimage.2017.08.031

Stucht, D., Danishad, K. A., Schulze, P., Godenschweger, F., Zaitsev, M., & Speck, O. (2015). Highest resolution in vivo human brain MRI using prospective motion correction. *PLoS ONE*, *10*(7), 1–17. https://doi.org/10.1371/journal.pone.0133921

Svanera, M., Benini, S., Bontempi, D., & Muckli, L. (2021). CEREBRUM-7T: Fast and Fully Volumetric Brain Segmentation of 7 Tesla MR Volumes. *Human brain mapping*, *42*(17), 5563–5580. https://doi.org/10.1002/hbm.25636

Tardif, C. L., Schäfer, A., Waehnert, M., Dinse, J., Turner, R., & Bazin, P. L. (2015). Multi-contrast multi-scale surface registration for improved alignment of cortical areas. *NeuroImage*, *111*, 107–122. https://doi.org/10.1016/j.neuroimage.2015.02.005

Trampel, R., Ott, D. V., & Turner, R. (2011). Do the congenitally blind have a stria of gennari? first intracortical insights in vivo. *Cerebral Cortex*, *21*(9), 2075–2081. https://doi.org/10.1093/cercor/bhq282

Turner, R. (2002). How much codex can a vein drain? Downstream dilution of activation-related cerebral blood oxygenation changes. *NeuroImage*, *16*(4), 1062–1067. https://doi.org/10.1006/nimg.2002.1082

Turner, R. (2013a). MRI Methods for In-Vivo Cortical Parcellation. In S. Geyer & R. Turner (Eds.), *Microstructural parcellation of the human cerebral cortex* (pp. 197–220). Springer. https://doi.org/10.1007/978-3-642-37824-9

Turner, R. (2013b). Where Matters: New Approaches to Brain Analysis. In S. Geyer & R. Turner (Eds.), *Microstructural parcellation of the human cerebral cortex* (pp. 179–196). Springer. https://doi.org/10.1007/978-3-642-37824-9

Turner, R., Oros-Peusquens, A. M., Romanzetti, S., Zilles, K., & Shah, N. J. (2008). Optimised in vivo visualisation of cortical structures in the human brain at 3 T using IR-TSE. *Magnetic Resonance Imaging*, *26*(7), 935–942. https://doi.org/10.1016/j.mri.2008.01.043

Uludag, K., Müller-Bierl, B., & Ugurbil, K. (2009). An integrative model for neuronal activity-induced signal changes for gradient and spin echo functional imaging. *NeuroImage*, *48*(1), 150–65. https://doi.org/10.1016/j.neuroimage.2009.05.051

Van Der Walt, S., Colbert, S. C., & Varoquaux, G. (2011). The NumPy array: a structure for efficient numerical computation. *Computing in Science & Engineering*, *13*(2), 22–30.

Waehnert, M. D., Dinse, J., Weiss, M., Streicher, M. N., Waehnert, P., Geyer, S., Turner, R., & Bazin, P.-L. (2014). Anatomically motivated modeling of cortical laminae. *NeuroImage*, *93 Pt 2*, 210–20. https://doi.org/10.1016/j.neuroimage.2013.03.078

Wallace, M. N., Cronin, M. J., Bowtell, R. W., Scott, I. S., Palmer, A. R., & Gowland, P. A. (2016). Histological Basis of Laminar MRI Patterns in High Resolution Images of Fixed Human Auditory Cortex. *Frontiers in neuroscience*, *10*(OCT), 455. https://doi.org/10.3389/fnins.2016.00455

Wallace, M. N., Johnston, P. W., & Palmer, A. R. (2002). Histochemical identification of cortical areas in the auditory region of the human brain. *Experimental Brain Research*, *143*(4), 499–508. https://doi.org/10.1007/s00221-002-1014-z

Wasserthal, C., Brechmann, A., Stadler, J., Fischl, B., & Engel, K. (2014). Localizing the human primary auditory cortex in vivo using structural MRI. *NeuroImage*, *93 Pt 2*(P1), 237–51. https://doi.org/10.1016/j.neuroimage.2013.07.046

Wehrli, F. W. (1990). Time-of-flight effects in MR imaging of flow. *Magnetic resonance in medicine*, *14*(2), 187–93. https://doi.org/10.1002/mrm.1910140205

Winawer, J., Sayres, R. A., & Wandell, B. A. (2010). Mapping hV4 and ventral occipital cortex. *10*, 1–22. https://doi.org/10.1167/10.5.1.Introduction

Ye, J. C. (2019). Compressed sensing MRI: a review from signal processing perspective. *BMC Biomedical Engineering*, *1*(1), 1–17. https://doi.org/10.1186/s42490-019-0006-z

Yushkevich, P. A., Piven, J., Hazlett, H. C., Smith, R. G., Ho, S., Gee, J. C., & Gerig, G. (2006). User-guided 3D active contour segmentation of anatomical structures: significantly improved efficiency and reliability. *NeuroImage*, *31*(3), 1116–28. https://doi.org/10.1016/j.neuroimage.2006.01.015

Yushkevich, P. A., Pluta, J., Wang, H., Wisse, L. E., Das, S., & Wolk, D. (2016). IC-P-174: Fast Automatic Segmentation of Hippocampal Subfields and Medial Temporal Lobe Subregions In 3 Tesla and 7 Tesla T2-Weighted MRI. *Alzheimer's & Dementia*, *12*(7S_Part_2), P126–P127. https://doi.org/10.1016/j.jalz.2016.06.205

Zachlod, D., Rüttgers, B., Bludau, S., Mohlberg, H., Langner, R., Zilles, K., & Amunts, K. (2020). Four new cytoarchitectonic areas surrounding the primary and early auditory cortex in human brains. *Cortex*, *128*, 1–21. https://doi.org/10.1016/j.cortex.2020.02.021

Zaitsev, M., Akin, B., LeVan, P., & Knowles, B. R. (2017). Prospective motion correction in functional MRI. *NeuroImage*, *154*(November 2016), 33–42. https://doi.org/10.1016/j.neuroimage.2016.11.014

Zaitsev, M., Maclaren, J., & Herbst, M. (2015). Motion artifacts in MRI: A complex problem with many partial solutions. https://doi.org/10.1002/jmri.24850

Zhang, X., Petersen, E. T., Ghariq, E., De Vis, J. B., Webb, A. G., Teeuwisse, W. M., Hendrikse, J., & Van Osch, M. J. (2013). In vivo blood T1 measurements at 1.5 T, 3 T, and 7 T. *Magnetic Resonance in Medicine*, *70*(4), 1082–1086. https://doi.org/10.1002/mrm.24550

Zwanenburg, J. J. M., Versluis, M. J., Luijten, P. R., & Petridou, N. (2011). Fast high resolution whole brain T2* weighted imaging using echo planar imaging at 7T. *NeuroImage*, *56*(4), 1902–7. https://doi.org/10.1016/j.neuroimage.2011.03.046

Supplementary Material

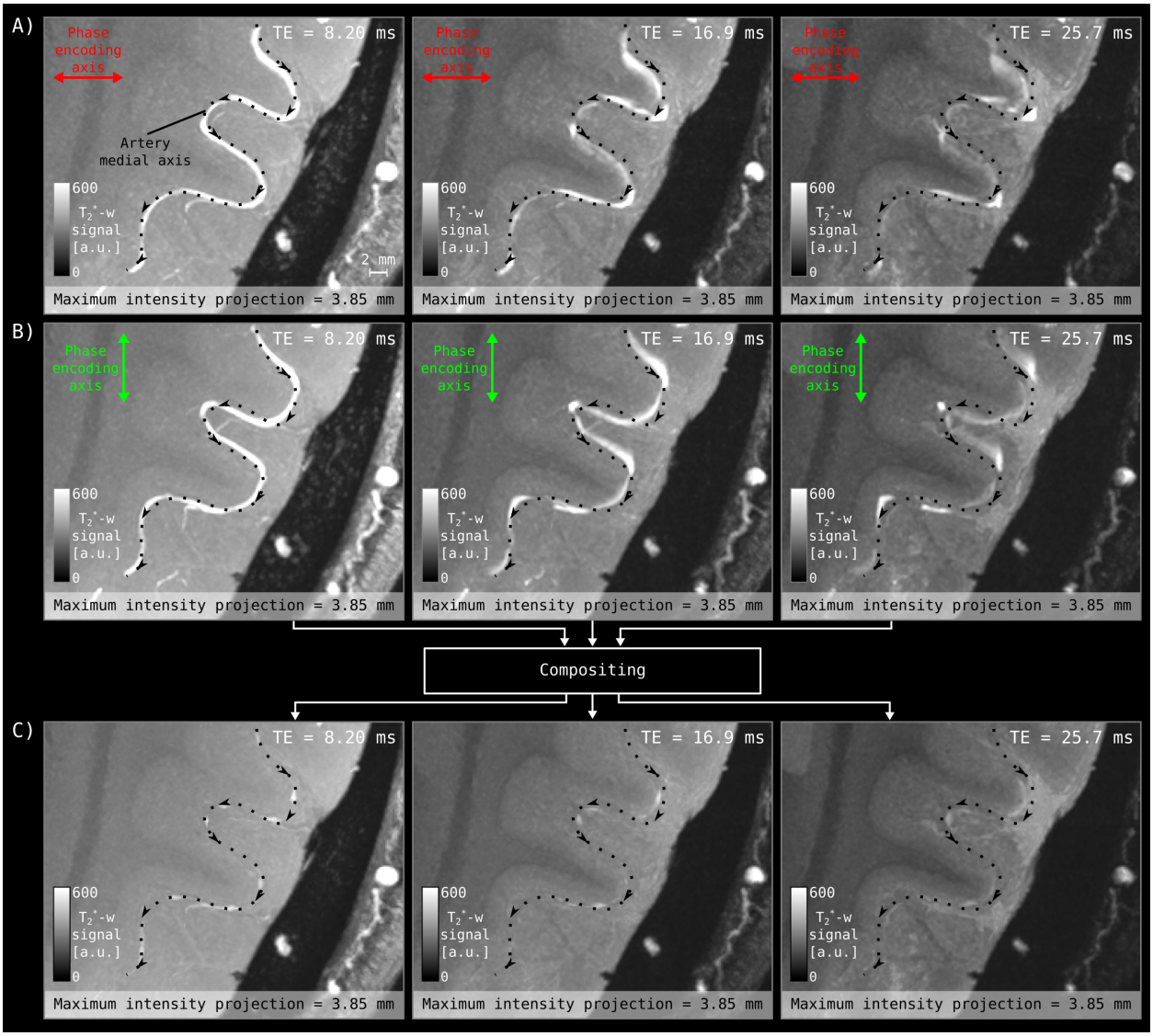

Supplementary Figure 1: Compositing method to mitigate blood motion artifacts in T_2^* -weighted images. Here we show results from an example participant (sub-03). **(A)** Zoomed-in view of three of the six echos acquired using the right-left phase encoding axis. **(B)** Same echos acquired using anterior-posterior phase encoding axis. See that the blood motion artifact appears along the vector component of the blood flow along the readout axis (which is perpendicular to the phase-encoding axis). **(C)** Result of compositing the acquired images using the minimum operator. We show maximum intensity projection over a small slab (see the first panel for the scale bar) in order to enhance the visibility of the arterial signal. The dotted line superimposed on all images indicates the medial axis of an artery that was manually identified from the shortest TE (3.83 ms) image where the blood motion artifact is minimal.

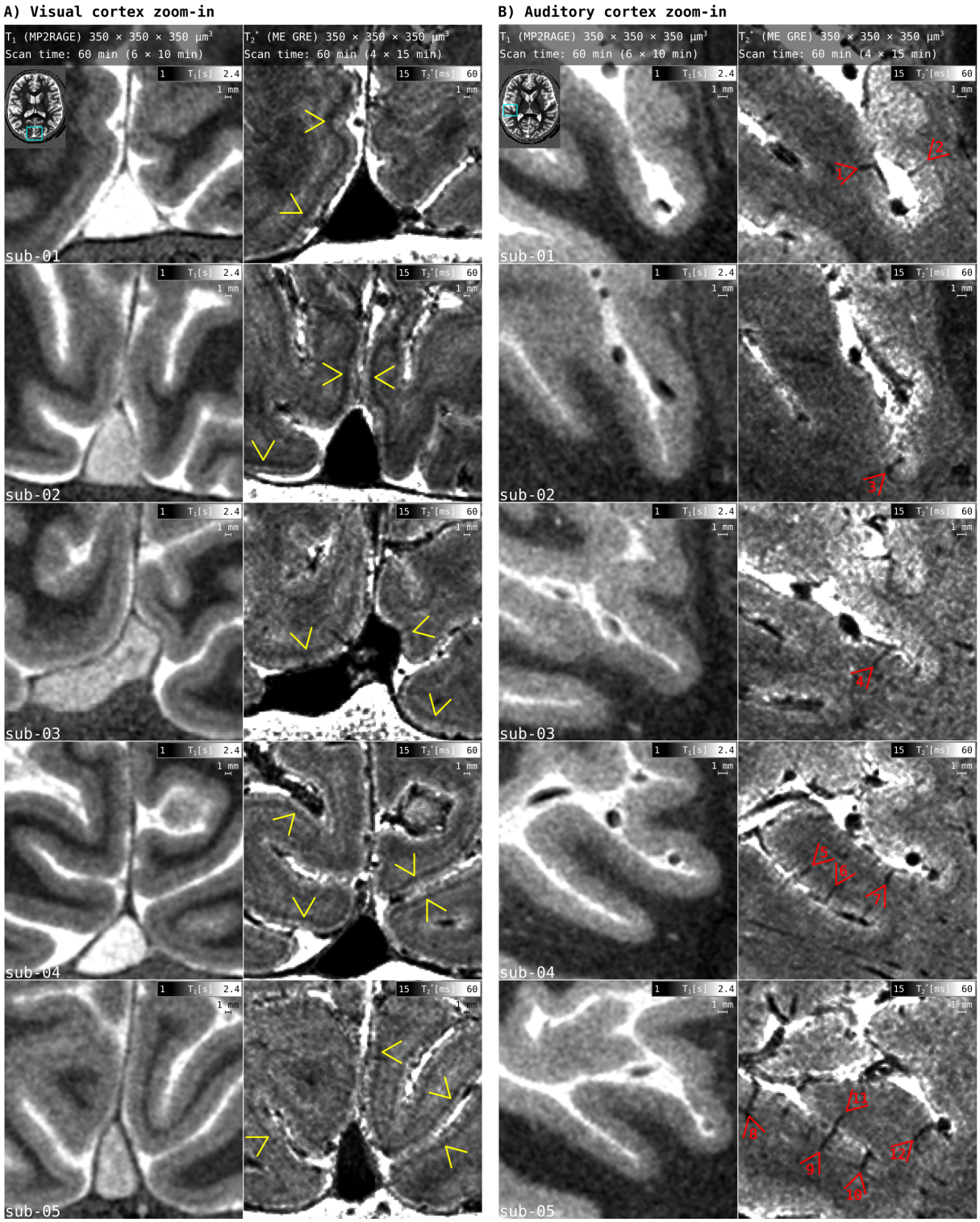

Supplementary Figure 2: Data quality after preprocessing. Yellow arrows point towards the stria of Gennari. Red arrows point towards intracortical vessels. Arrows 1 & 4 highlight cases in which part of a vessel lies on top of the gray matter. Arrows 9 & 11 highlight cases in which a common vein collects blood from two opposite gray matter chunks. Arrow 12 highlights a case where a smaller vessel connects to a large vein lying at the bottom of a sulcus.

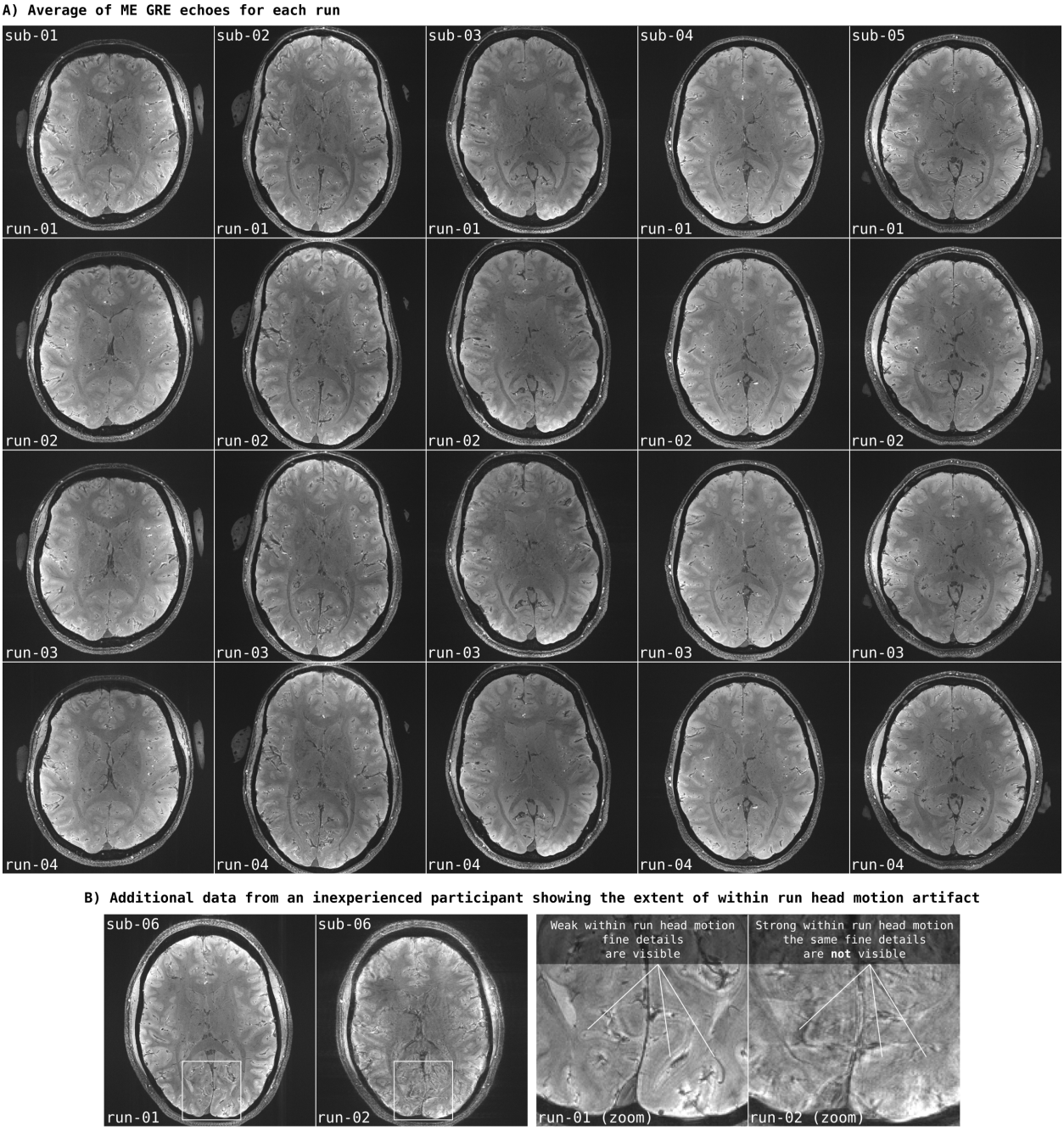

Supplementary Figure 3: ME GRE data quality for each run before preprocessing. (A) Here we show the average of all echoes at the middle slice of each acquisition. Given the high quality of these data, we ended up discarding no individual runs. (B) Additional data acquired from an inexperienced participant (who did not complete the scanning sessions) to demonstrate within run head motion artifacts (we did not process or analyze this data further). When a participant moves too much during data acquisition, the resulting images have specific types of blur artifacts. Typical approaches to mitigate head motion include prospective motion correction and/or preselecting participants who are able to keep their head still [REF: Discussion Section]. In the present study, we have employed participant preselection in combination with "fMRI-style" 10-15 minute long single data acquisition run.

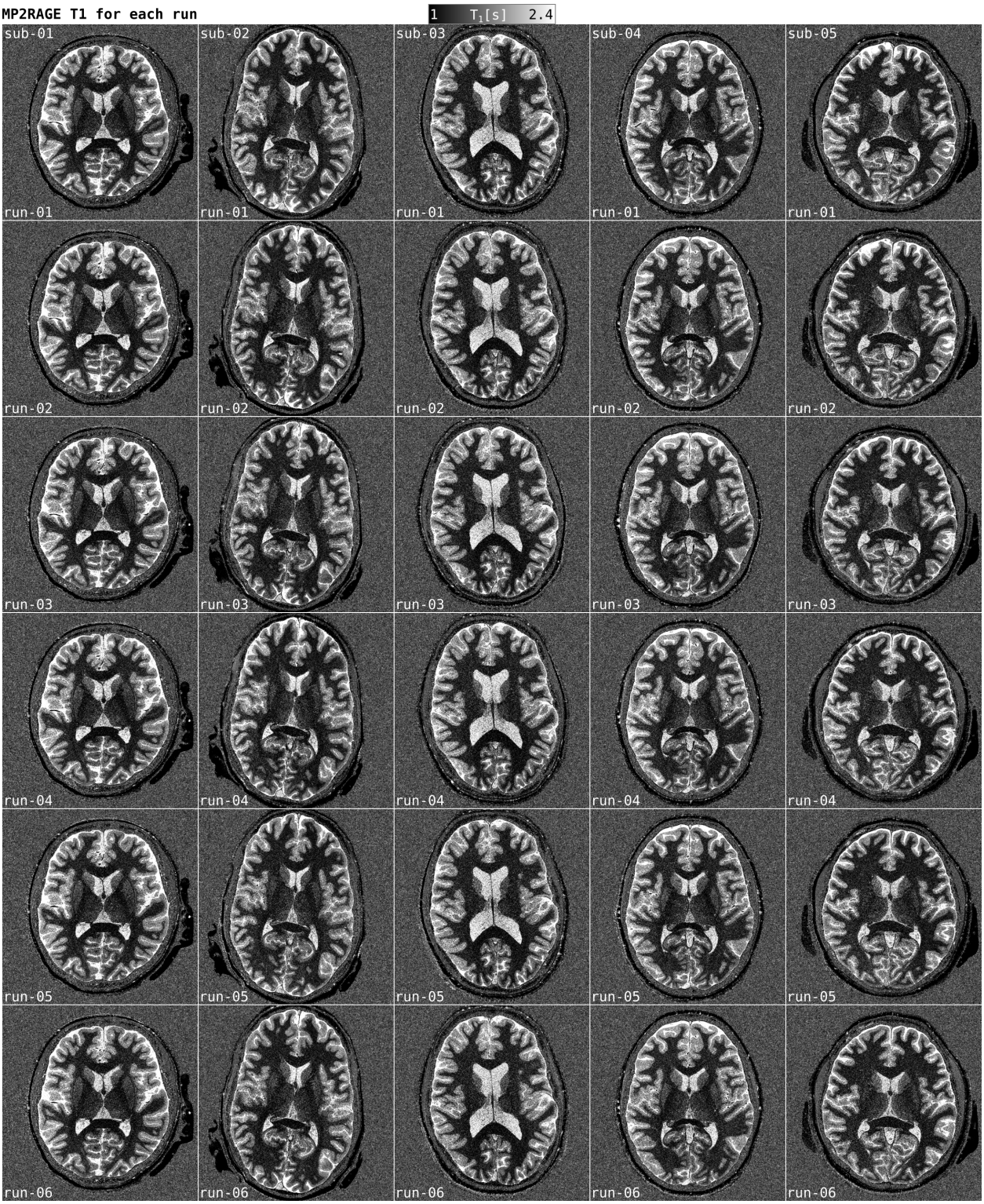

Supplementary Figure 4: MP2RAGE data quality for each run before preprocessing. Here we show MP2RAGE T_1 images at the middle slice of each acquisition. The same T_1 range shown in the colorbar on top is used for all panels. Given the consistent and high quality of these data (also see also Supplementary Figure 3), we ended up discarding no individual runs.

Supplementary Table 1: Acquisition details of mesoscopic T2 and T_2^* contrast MRI datasets. We have strictly selected articles that measure: (i) T2 or T_2^* contrasts, (ii) humans, (iii) *(*in vivo), and (iv) at voxel resolution less than 0.5 mm in at least two dimensions to qualify as "mesoscopic resolution". Here we summarize acquisition details of these articles (Budde et al., 2011; Duyn et al., 2007; Federau & Gallichan, 2016; Kemper et al., 2018; Lüsebrink et al., 2021; Mattern et al., 2018; Petridou et al., 2010; Sánchez-Panchuelo et al., 2012; Trampel et al., 2011; Zwanenburg et al., 2011). We included Koopmans et al. (2011) as a notable "near-mesoscopic" exception to our criteria (denoted by "*"). Interestingly, most articles did not measure quantitative T_2^* but rather preferred weighted imaging. "3D FatNavs" stands for "fat based motion navigators", "Preselection" stands for preselecting participants who are experienced in being scanned and can lie still inside the scanner consistently (this strategy is used and reported previously by Allen et al. (2022), Bollmann et al. (2022), and Tardif et al. (2015)). "N/A" indicates "not reported" or "not applicable". "?" indicates "cannot be computed given the reported details".

Article	Contrast	Pulse Seq.	Voxel size			Coverage	Quantitative MRI	Motion Correction	Open access to data
			X [mm]	Y [mm]	Z [mm]				
Duyn2007	T2*-w	GRE	0.24	0.24	1	Partial	No	N/A	No
Petridou2010	T2*-w	2D GRE	0.25	0.25	1.5	Partial	No	Retrospective	No
Budde2011	T2*	3D ME GRE	0.35	0.35	2	Partial	Yes	Retrospective	No
Koopmans2011*	T2*	3D ME GRE	0.75	0.75	0.75	Partial	Yes	Retrospective	No
Trampel2011	T2-w	TSE	0.5	0.5	0.5	Partial	No	N/A	No
Zwanenburg2011	T2*-w	3D GRE	0.5	0.5	0.5	Partial	No	Retrospective	No
Sanchez-Panchuelo2012	T2*	3D ME GRE	0.4	0.4	0.4	Partial	Yes	N/A	No
Federau2016	T2-w	TSE	0.38	0.38	0.38	Whole brain	No	3D FatNavs + Retrospective	Yes (https://osf.io/63qjk/)
Federau2016	T2*-w	GRE	0.35	0.35	0.35	Whole brain	No	3D FatNavs + Retrospective	Yes (https://osf.io/63qjk/)
Mattern2018	T2*-w	3D GRE	0.33	0.33	1.25	Whole brain	No	Prospective + Retrospective	No (but see Lüsebrink2021 for 0.33 mm iso. data)
Kemper2018	T2*-w	2D GRE	0.35	0.35	0.35	Partial	No	Retrospective	No
Lüsebrink2021	T2-w	TSE	0.45	0.45	0.45	Whole brain	No	Prospective + Retrospective	Yes (https://doi.org/10.18112/openneuro.ds003563.v1.0.1)
Lüsebrink2021	T2*-w	GRE	0.33	0.33	0.33	Whole brain	No	Prospective + Retrospective	Yes (https://doi.org/10.18112/openneuro.ds003563.v1.0.1)
Gülban2022	**T2***	**3D ME GRE**	**0.35**	**0.35**	**0.35**	**Partial**	**Yes**	**Preselection + Retrospective**	**Yes (https://doi.org/10.17605/OSF.IO/N5BJ7)**

Article	Contrast	Pulse Seq.	Voxel size			Voxel volume	Echoes	Slab volume	Partici-pants	Field strength	Scan duration		Total duration	Acceleration
			X [mm]	Y [mm]	Z [mm]	[µl]		[liter]		[Tesla]	[min]	[nr. avg.]	[min]	
Duyn2007	T2*-w	GRE	0.24	0.24	1	0.058	1	?	7	7	10	1	10	N/A
Petridou2010	T2*-w	2D GRE	0.25	0.25	1.5	0.094	1	0.5	6	7	3.6	3	11	N/A
Budde2011	T2*	3D ME GRE	0.35	0.35	2	0.245	5	0.9	5	9.4	10	2	20	GRAPPA = 2
Koopmans2011*	T2*	3D ME GRE	0.75	0.75	0.75	0.422	10	0.6	8	7	1.5	10	15	GRAPPA = 4
Trampel2011	T2-w	TSE	0.5	0.5	0.5	0.125	1	?	13	7	10	1	10	Turbo factor = 2
Zwanenburg2011	T2*-w	3D GRE	0.5	0.5	0.5	0.125	1	1.5	8	7	6	1	6	SENSE = 2.3, Partial Fourier = 0.78
Sanchez-Panchuelo2012	T2*	3D ME GRE	0.4	0.4	0.4	0.064	4	0.9	4	7	15	1	15	N/A
Federau2016	T2-w	TSE	0.38	0.38	0.38	0.055	1	4.0	1	7	26	2	52	PF = 3/4 in both PE dir., Turbo = 166
Federau2016	T2*-w	GRE	0.35	0.35	0.35	0.043	1	3.1	1	7	42	1	42	PF = 3/4 in both PE dir.
Mattern2018	T2*-w	3D GRE	0.33	0.33	1.25	0.136	1	3.7	4	7	18	1	18	N/A
Kemper2018	T2*-w	2D GRE	0.35	0.35	0.35	0.043	1	0.2	2	9.4	7	6	42	N/A
Lüsebrink2021	T2-w	TSE	0.45	0.45	0.45	0.091	1	6.3	1	7	23	1	23	GRAPPA = 3, PF = 6/8 in Slice dir., Turbo = 173
Lüsebrink2021	T2*-w	GRE	0.33	0.33	0.33	0.036	1	4.9	1	7	43	4	172	PF = 6/8 in PE dir. and in Slice dir.
Gülban2022	**T2***	**3D ME GRE**	**0.35**	**0.35**	**0.35**	**0.043**	**6**	**1.5**	**5**	**7**	**15**	**4**	**60**	**GRAPPA = 2**